

# IL-7 Engages Multiple Mechanisms to Overcome Chronic Viral Infection and Limit Organ Pathology

Marc Pellegrini,<sup>1,2,3,10</sup> Thomas Calzascia,<sup>3,10</sup> Jesse G. Toe,<sup>1</sup> Simon P. Preston,<sup>1</sup> Amy E. Lin,<sup>3</sup> Alisha R. Elford,<sup>3</sup> Arda Shahinian,<sup>3</sup> Philipp A. Lang,<sup>3</sup> Karl S. Lang,<sup>3</sup> Michel Morre,<sup>4</sup> Brigitte Assouline,<sup>4</sup> Katharina Lahl,<sup>5</sup> Tim Sparwasser,<sup>6</sup> Thomas F. Tedder,<sup>7</sup> Ji-hye Paik,<sup>8</sup> Ronald A. DePinho,<sup>8</sup> Sameh Basta,<sup>9</sup> Pamela S. Ohashi,<sup>3,11,\*</sup> and Tak W. Mak<sup>3,11</sup>

<sup>1</sup>The Walter and Eliza Hall Institute of Medical Research, Melbourne, VIC 3052, Australia

<sup>2</sup>Department of Medical Biology, University of Melbourne, Melbourne 3050, Australia

<sup>3</sup>Departments of Medical Biophysics and Immunology, Campbell Family Cancer Research Institute, Ontario Cancer Institute, University Health Network, Toronto, Ontario M5G 2C1, Canada

<sup>4</sup>Cytheris Inc., 92130 Issy les Moulineaux, France

<sup>5</sup>Laboratory of Immunology and Vascular Biology, Department of Pathology, Stanford University School of Medicine, Stanford, CA 94305, USA

<sup>6</sup>Institute for Infection Immunology, TWINCORE, Centre for Experimental and Clinical Infection Research, Feodor-Lynen-Str.7, 30625 Hannover, Germany

<sup>7</sup>Department of Immunology, Duke University Medical Center, Durham, NC 27708, USA

<sup>8</sup>Belfer Institute for Applied Cancer Science, Department of Medical Oncology, Department of Medicine and Department of Genetics, Dana-Farber Cancer Institute, Harvard Medical School, Boston, MA 02115, USA

<sup>9</sup>Department of Microbiology and Immunology, Queen's University, Kingston, ON K7L 396, Canada

<sup>10</sup>These authors contributed equally to this work

<sup>11</sup>These authors contributed equally to this work

\*Correspondence: [pohashi@uhnres.utoronto.ca](mailto:pohashi@uhnres.utoronto.ca)

DOI 10.1016/j.cell.2011.01.011

## SUMMARY

Understanding the factors that impede immune responses to persistent viruses is essential in designing therapies for HIV infection. Mice infected with LCMV clone-13 have persistent high-level viremia and a dysfunctional immune response. Interleukin-7, a cytokine that is critical for immune development and homeostasis, was used here to promote immunity toward clone-13, enabling elucidation of the inhibitory pathways underlying impaired antiviral immune response. Mechanistically, IL-7 downregulated a critical repressor of cytokine signaling, *Socs3*, resulting in amplified cytokine production, increased T cell effector function and numbers, and viral clearance. IL-7 enhanced thymic output to expand the naive T cell pool, including T cells that were not LCMV specific. Additionally, IL-7 promoted production of cytoprotective IL-22 that abrogated liver pathology. The IL-7-mediated effects were dependent on endogenous IL-6. These attributes of IL-7 have profound implications for its use as a therapeutic in the treatment of chronic viral diseases.

## INTRODUCTION

Much attention has focused on modulating immune responses in an attempt to promote clearance of chronic viral infections. This

is particularly relevant to human immunodeficiency virus (HIV) infections in which the immune system fails to clear virus and eventually succumbs to uncontrolled viral turnover (Day et al., 2006; Klenerman and Hill, 2005). Understanding the mechanisms that circumvent immune responses in cases of overwhelming viral replication and antigen expression underlies any rational attempt to augment immunity in HIV infection.

Lymphocytic choriomeningitis virus (LCMV) variant clone 13 establishes a chronic infection in mice with high viral turnover, hence mimicking the massive viral antigen levels associated with HIV infection in humans (Wherry et al., 2003). Clone 13 infection has served as a powerful tool in characterizing the dysfunctional immune response associated with chronic viremia, and numerous parallels with HIV, HCV, and HBV infection have been described (reviewed in Wilson and Brooks [2010]). In contrast to clone 13, LCMV Armstrong causes an acute infection in C57Bl/6 mice, and the immune response differs significantly from clone 13 infection both in magnitude and also in the specificity of the responding immunodominant CD8 T cell clones (Wherry et al., 2003). In Armstrong infection, the most prominent and highest-affinity CD8 T cell response is directed against the dominant nucleoprotein NP396 epitope, followed by the glycopeptide GP33 epitope and then by GP276. Clone 13 infection is characterized by a deletion of the high-affinity NP396 clones and potentially a functional defect in the remaining LCMV-specific T cells clones (Wherry et al., 2003). Similar phenotypic and functional disturbances have been described in T cells of HIV-infected humans (Day et al., 2006).

Several host inhibitory pathways, which may circumvent effective immune responses, have been identified in mice that

are chronically infected with LCMV clone 13 (Barber et al., 2006; Brooks et al., 2006; Ejrnaes et al., 2006; Matter et al., 2006). We hypothesized that nonredundant cytokines involved in homeostatic proliferation, and therefore apt at overcoming inhibitory networks that naturally limit expansion, would offer the most promise in promoting immune responses. IL-7 is unique for its critical and nonredundant role in immune development and homeostasis and therefore is a prime candidate for use as an immunotherapeutic to overcome immune inhibitory networks in chronic active infections. Indeed, IL-7 offers significant therapeutic promise (Levy et al., 2009; Sereti et al., 2009; Sportès et al., 2008). It has been used in several nonhuman primate SIV infection models that have demonstrated its diverse immunological effects (Beq et al., 2006; Fry et al., 2003; Nugeyre et al., 2003). However, the efficacy of IL-7 in promoting viral clearance has not been fully explored. Importantly, the ability of IL-7 to antagonize immune inhibitory networks and the mechanism underlying its immune modulatory actions remains an area of active investigation. Such knowledge holds the potential to illuminate points for rational therapeutic intervention.

In this study, administration of recombinant human IL-7 to mice that are chronically infected with clone 13 increased the magnitude of the immune response with rescue of the NP396-specific T cell clones. It increased the size of the naive T cell pool, including T cell clones directed against non-LCMV specific epitopes, in part by increasing thymic output. LCMV clone 13-specific T cells showed enhanced degranulation kinetics and cytokine production with IL-7 therapy, resulting in effective viral clearance and a downregulation of PD-1 on effector T cells. In addition, IL-7 promoted a cytokine milieu favoring immune activation and production of the cytoprotective cytokine IL-22, thus limiting hepatotoxicity. At the molecular level, IL-7 downregulated suppressor of cytokine signaling 3 (Socs3) expression in T cells. This was mediated by suppression of FoxO transcription factors. We show that conditional deficiency of Socs3 in T cells replicates aspects of the IL-7-induced phenotype in mice that are infected with LCMV clone 13. These findings have major implications for our understanding of chronic viremia and the therapeutic use of IL-7.

## RESULTS

### IL-7 Increases Antiviral T Effector Responses and Organ Infiltration in Clone 13 Infection

Clone 13-infected mice were treated with IL-7 or PBS commencing 8 days after infection, when chronicity had been established. After 3 weeks of IL-7 therapy, the total number of splenic CD8 and CD4 T cells was increased 11- and 5-fold, respectively, compared to PBS control animals (Figure 1A). IL-7 treatment did not alter the number of granulocytes, macrophages, or dendritic cells (DCs) compared to controls. A dramatic 10- to 25-fold increase in virus-specific CD8 T cells recognizing GP276 and GP33, respectively, was observed in IL-7-treated mice compared to controls (Figure 1B). An equally robust 10-fold increase in NP396-specific T cells, which represented a very small proportion of virus-specific cells in control animals, was also observed (Figure 1B). The increase in splenic CD8 and CD4 T cell numbers and virus-specific T cells tracked

with an equivalent increase in liver, kidney, brain, and lung infiltration by lymphocytes and virus-specific T cells (Figures 1C and 1D and data not shown). Therefore, IL-7 is able to expand and rescue T cell numbers, including CD8 T cell clones that are normally deleted in clone 13 infection, resulting in efficient lymphocyte infiltration into infected organs.

### Enhanced Function of Virus-Specific T Cells, Viral Clearance, and Downregulation of PD-1 with IL-7 Treatment

To verify that the large increase in clone 13-specific T cells in IL-7-treated animals translated to a functional gain, we examined their ex vivo capacity to degranulate and produce cytokines. We observed a 2-fold increase in the proportion of clone 13-specific CD8 T cells in IL-7-treated animals at day 29 postinfection that were able to produce cytokines and degranulate in restimulation assays compared to controls (Figure 2A). This translates to a massive 30- to 50-fold increase in the number of functional GP33-specific splenic CD8 T cells in IL-7-treated animals compared to controls (Figure 2A). Similarly, the proportion of clone 13-specific CD4 T cells recognizing GP61 that produce both IFN $\gamma$  and IL-2 was 4-fold higher in IL-7-treated animals compared to controls (Figure 2B). This translates to a 20-fold increase in the absolute number of functional CD4 T cells recognizing GP61 in the spleens of IL-7-treated animals (Figure 2B). These results highlight the potent effects of IL-7 treatment on the total number of functional CD8 and CD4 virus-specific T cells in a model of chronic infection.

Recently, high PD-1 levels on T cells from clone 13-infected animals have been shown to correlate with a dysfunctional phenotype (Barber et al., 2006). We thus examined the level of PD-1 expression on both CD8 and CD4 T cells from IL-7- and PBS-treated animals and observed lower levels of PD-1 on both CD8 and CD4 T cells expressing this receptor, and hence activated by antigen, in IL-7-treated animals compared to controls (Figures 2C and 2D). Furthermore, an acute activation marker, CD69, was downregulated on PD-1-expressing T cells from IL-7-treated animals (Figures 2C and 2D). Collectively, these data indicate that clone 13-specific CD4 and CD8 T cells in IL-7-treated mice begin to lose their activation phenotype by day 29 after 3 weeks of therapy, most likely due to viral clearance. Indeed, IL-7 treatment facilitated viral clearance from spleen and liver by days 22–29 postinfection and resulted in elimination of virus from chronic reservoirs, including brain, lung, and kidney between days 36 and day 60 (Figure 2E). Control animals were not able to clear virus by the end of follow-up at day 60, consistent with previous reports that have demonstrated long-term chronicity in clone 13-infected mice (Wherry et al., 2003).

### CD4 and CD8 T Cells, but Not B Cells, Are Required for IL-7's Capacity to Clear Virus

In addition to the expansion of activated T cells, IL-7 caused an increase in B cell numbers in infected mice. However, proportionally, T cells represented the largest increase in lymphocyte numbers (Figure S1 available online and Figure 1A). To determine which of the expanded lymphocyte populations may contribute to enhanced clearance of virus, we depleted the various subsets during the course of IL-7 therapy to maintain CD4 or CD8 T cell

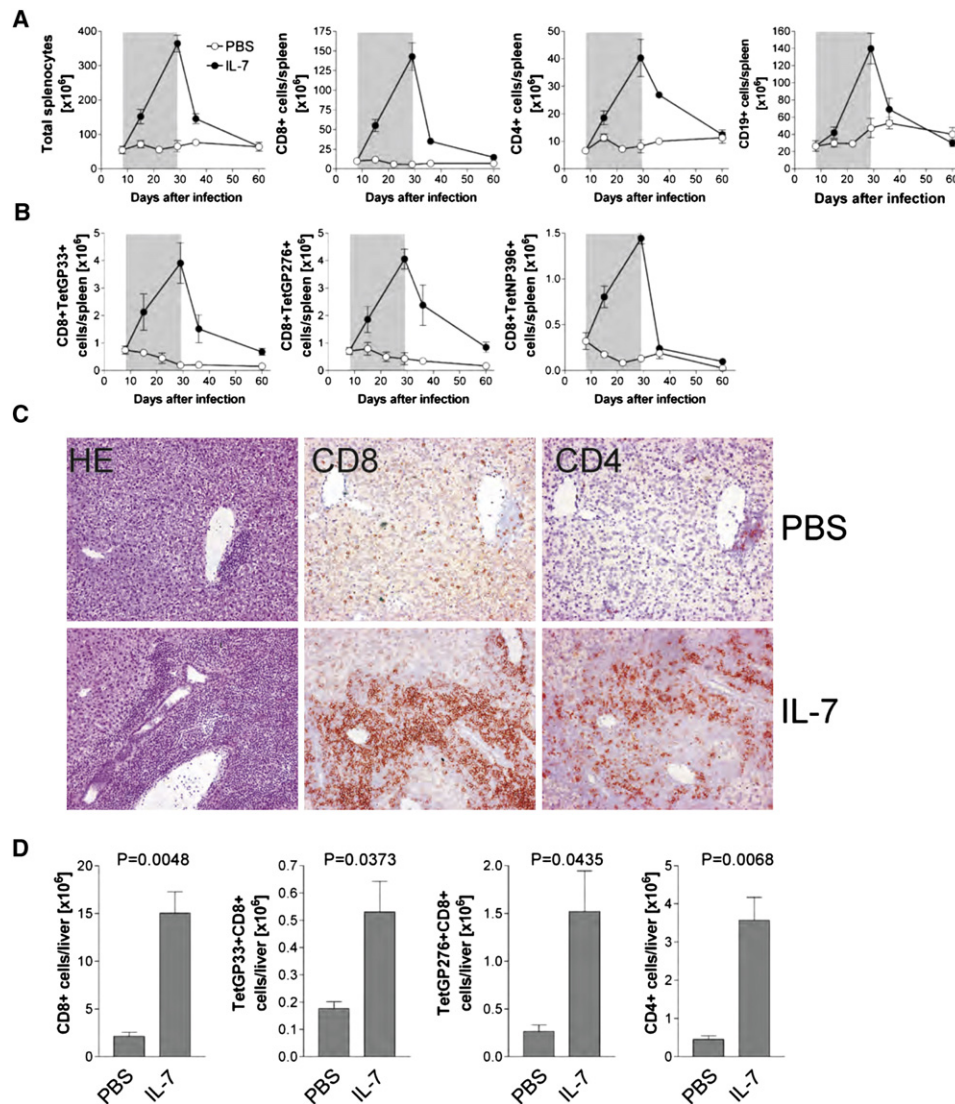


**Figure 1. IL-7 Augments Antiviral Responses and Organ Infiltration in Chronic Clone 13 Infection**

(A) The absolute number of cells was quantified in infected mice. The gray shaded bars indicate duration of IL-7 or PBS therapy. The experiment was repeated three times, and data was pooled with error bars indicating SEM ( $n = 12$  for each group and time).

(B) The absolute number of LCMV-specific CD8 T cells was quantified by tetramer staining. Data were obtained from four animals in each group and at each time point. The experiment was repeated three times, and data were pooled with error bars indicating SEM ( $n = 12$  for each group and time).

(C) Immunohistochemistry showing CD4 and CD8 infiltration in liver sections after 3 weeks of IL-7 or PBS therapy in clone 13-infected mice. These sections are representative of more than 12 analyzed histological specimens.

(D) Number of infiltrating virus-specific CD8 T cells in livers of IL-7- or PBS-treated clone 13-infected animals after 3 weeks of therapy. Bars represent averages with SEM from data obtained from six mice in each group. The experiment was repeated twice.

See also Figure S1.

numbers at the same level as PBS clone 13-infected control mice (data not shown). Depletion of either CD4 or CD8 T cells abrogated IL-7's ability to clear virus (Figure S2).

Similarly, we depleted B cells with an anti-CD20 mAb (Uchida et al., 2004) during the course of IL-7 treatment (Figure S2A). Despite this depletion of B cells, the effects of IL-7 on viral clearance were not diminished (Figure S2B). This is consistent with previous studies showing that B cells play only minor roles in modulating T cell responses in cases in which there is abundant antigen (Bouaziz et al., 2007). Our data clearly demonstrate that

IL-7 exerts its effect on viral clearance through the modulation of T cells rather than B cells. This has important implications in translating IL-7 therapies to humans, as this cytokine does not expand B cells in humans (Rosenberg et al., 2006).

#### IL-7 Expands Non-LCMV-Specific Naive T Cell Numbers in Clone 13-Infected Mice

We observed that the majority of splenic CD8 T cells in clone 13-infected mice treated with IL-7 or PBS expressed high levels of CD44 (Figure 3A and data not shown). We speculated that only

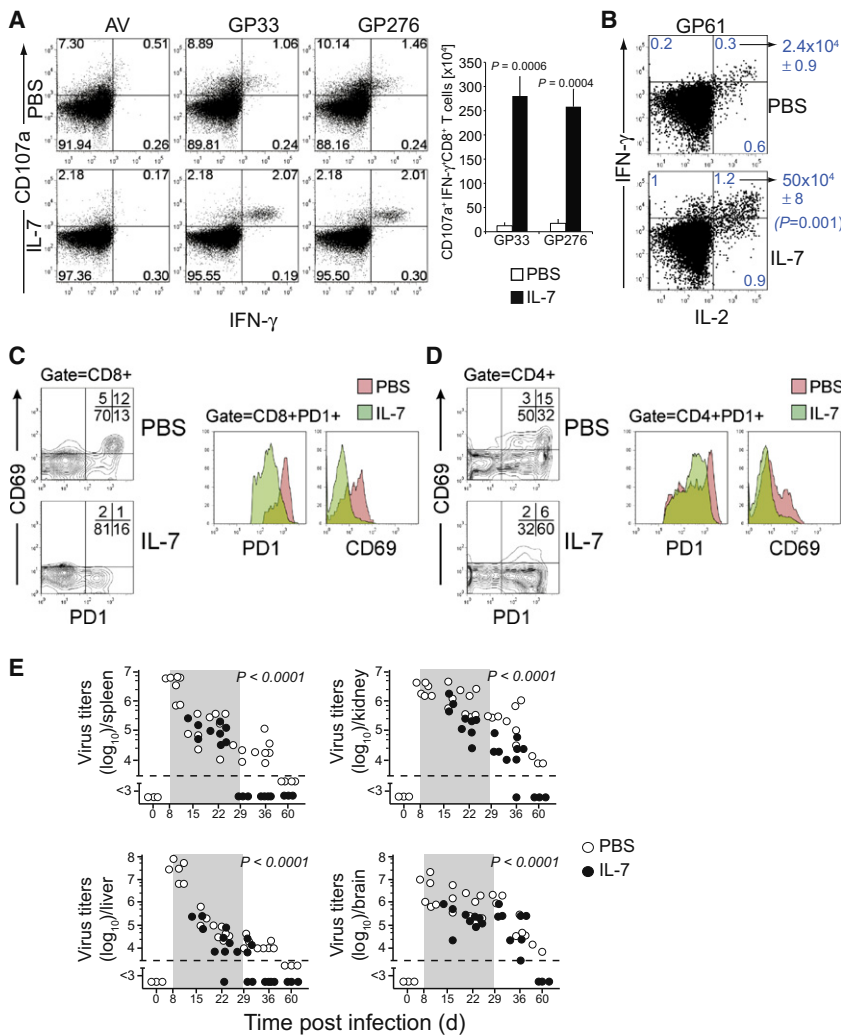


**Figure 2. IL-7 Therapy Enhances T Cell Function and Facilitates Viral Elimination with Downregulation of PD-1 and Acute Activation Markers on CD4 and CD8 T Cells**

(A) Direct ex vivo degranulation (CD107a) and cytokine production in virus-specific CD8 T cells during clone 13 infection. Dot plots, gated on CD8 T cells, are representative of 12 independent analyses performed after restimulation of splenocytes with cognate peptides or control peptide at the completion of IL-7 or PBS in vivo treatment. (Right) Bar graph shows average cell numbers and SEM.

(B) Cytokine production in virus-specific CD4 T cells during clone 13 infection. Dot plots, gated on CD4 T cells, are representative of 12 independent analyses performed after restimulation of splenocytes with cognate peptide at the completion of IL-7 or PBS in vivo treatment. Averages and SEM, right arrow, indicate absolute splenic CD4 T cell numbers secreting both IFN- $\gamma$  and IL-2.

(C and D) Histograms show the expression level of markers on either CD8<sup>+</sup>PD1<sup>+</sup> (C) or CD4<sup>+</sup>PD1<sup>+</sup> (D) splenic T cells obtained from animals receiving IL-7 or PBS for 3 weeks. Contour plots and histograms are representative of more than 12 analyses performed on independent mice.

(E) Organ viral titers in IL-7- or PBS-treated clone 13-infected mice. The gray bars represent duration of therapy, and dotted lines represent the reliable limit of detection for viral plaque assay. Significance (p values) was determined using a time to event analysis and log rank test.

See also Figure S2.

a fraction of these cells were actually LCMV specific, and the remainder were non-LCMV-specific naive T cells that were upregulating CD44 in response to the inflammatory environment. This was supported, in the case of IL-7-treated animals, by the fact that only 15% of the expanded CD8 T cell population, most of which are CD44<sup>hi</sup> (data not shown) also expressed PD-1, which represents an antigen-driven activation marker (Figure 3B). To examine this further, we purified, phenotyped, and quantified CD8 T cells recognizing non-LCMV-specific epitopes directed against the SV40 large T antigen and the ovalbumin-derived SIINFEKL epitope (using pooled SV40/ova tetramers). These cells were expanded more than 14-fold in IL-7-treated animals compared to controls, and in both cases, although to a greater extent with IL-7 treatment, the levels of CD44 were upregulated on these cells following clone 13 infection (Figure 3C). Consistent with the fact that these cells were not activated by TCR triggering, as opposed to GP33 virus-specific T cells, there was minimal or no upregulation of PD-1 expression, hence indicating their naive origins (Figure 3C). Collectively, these data support the view that, in addition to expanding the number of activated

virus-specific CD8 T cells, IL-7 also greatly expands the naive T cell pool, including T cells recognizing nonviral-related epitopes in chronically infected mice.

A similar finding has been reported with the use of IL-7 in uninfected humans

(Sportès et al., 2008), but our data show that these effects are eminently translatable to chronic viral infections. These findings have important implications for the use of IL-7 in HIV-infected patients in which T cells of many different specificities unrelated to HIV also succumb to the disease (Li et al., 2005; Mattapallil et al., 2005). It is unlikely that the expansion of naive T cells contributes significantly to the clearance of virus in our model, as IL-7 is administered at the peak of immune activation, and its predominant effect is expansion of activated LCMV-specific T cells (Figure 3B).

**IL-7 Enhances Thymic Output during Chronic Viral Infection to Expand the Naive T Cell Pool**

The expanded naive T cell pool that we observed with IL-7 therapy may be a result of increased thymic output and/or peripheral expansion. IL-7 is thought to mobilize recent thymic emigrants from lymphoid tissues and promote thymic egress (Chu et al., 2004; Sportès et al., 2008). However, there is no detailed analysis of thymic and peripheral effects on recent thymic emigrants in the setting of chronic viral infection. To



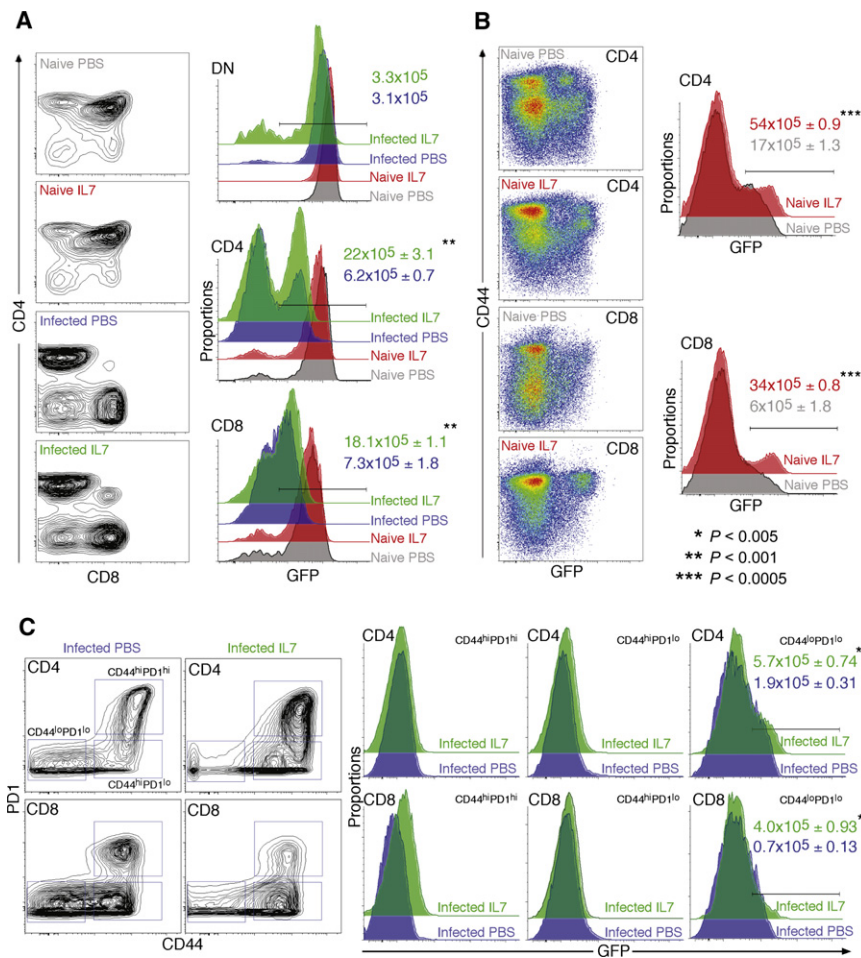


**Figure 4. IL-7 Increases Thymic Output during Chronic Viral Infection and Promotes Recent Thymic Emigrants in the Periphery**

(A) Rag-GFP mice were used to track recent thymic emigrants. Infected and uninfected mice were treated with IL-7 or PBS for 5 days (starting 8 days after infection in the former group). Numbers represent averages and SD of the total number of GFP<sup>+</sup> cells in the thymus that are double negative (DN), CD4 positive, or CD8 positive as indicated. Green represents data from infected IL-7-treated animals, and blue represents data from infected PBS-treated animals. Data were collected from four animals in each group, and the experiment was repeated twice.

(B) Numbers of recent thymic emigrants in the periphery of naive uninfected mice. Dot plots and histograms show the number of GFP<sup>+</sup> cells (representing recent thymic emigrants in Rag-GFP mice) in the periphery of uninfected mice treated with PBS or IL-7 for 5 days. Numbers represent averages and SD of data collected from four animals in each group, and the experiment was repeated twice. Red represents data from naive IL-7-treated animals, and gray represents data from naive PBS-treated animals.

(C) Numbers of recent thymic emigrants in the periphery of clone 13-infected mice. Contour plots and histograms show the number of GFP<sup>+</sup> cells (representing recent thymic emigrants in Rag-GFP mice) in the periphery of clone 13-infected mice treated with PBS or IL-7 for 5 days starting 8 days after infection. Each histogram corresponds to the designated gated population shown in the dot plots (left). Numbers represent averages and SD of data collected from four animals in each group, and the experiment was repeated twice. Green represents data from infected IL-7-treated animals, and blue represents data from naive PBS-treated animals. Asterisks represent p values as indicated.

in GFP bright CD8 and CD4 single positive thymocytes may reflect a simple local thymic proliferation of newly generated CD8 and CD4 thymocytes. However, it may also be possible that enhanced thymopoiesis with de novo production of new single positive cells may contribute to the increased number of these cells in the thymus. Among the peripheral T cell population, in both uninfected and clone 13-infected animals, IL-7 increased the number of CD4 and CD8 single positive recent thymic emigrants by 3- to 6-fold, respectively (Figures 4B and 4C). These GFP<sup>+</sup> cells were CD44<sup>lo</sup>PD-1<sup>lo</sup>, indicating that they were truly naive and recent emigrants to the periphery (Figure 4C). These data show that IL-7 therapy in the setting of chronic infection can substantially expand the peripheral T cell pool both through mechanisms of peripheral homeostasis and enhanced thymic output.

**IL-7 Augments IL-6, IL-12, IL-17, and IFN $\gamma$  Serum Levels while Limiting TGF- $\beta$  Levels**

We investigated the serum cytokine levels associated with the increased numbers of lymphocytes in IL-7-treated clone 13-infected mice. We found that the levels of several proinflam-

matory cytokines are greatly increased, particularly IL-6, IL-17, and IFN $\gamma$  in IL-7-treated infected mice (Figure 5A). However, there was a modest decrease in the levels of TGF $\beta$  (Figure 5A). The large increase in IL-17 serum levels likely reflects an expansion of Th17 cells, which may be a consequence of an IL-7-induced shift favoring IL-6 levels over TGF $\beta$  and, in turn, favoring Th17 over T regulatory (Treg) cell differentiation (Ogura et al., 2008; Zhou et al., 2008). Interestingly, we observed a 2-fold increase in IL-10 serum levels at later time points during IL-7 treatment compared to controls (Figure 5A). Previous work suggests that IL-10 may abrogate immunity to chronic viruses, but in the present study, this inhibitory effect is likely overshadowed by the 17- to 18-fold increase in proinflammatory cytokines (Brooks et al., 2006; Ejrnaes et al., 2006). Despite the dramatic increases in proinflammatory cytokines and the heavy infiltration seen in organs of IL-7-treated animals (Figure 1C), we did not observe any significant immune-mediated pathology such as hepatitis (Figure 5B). Collectively, these data show that IL-7 promotes a proinflammatory milieu while limiting cytotoxicity and decreasing the levels of the inhibitory cytokine TGF $\beta$ .

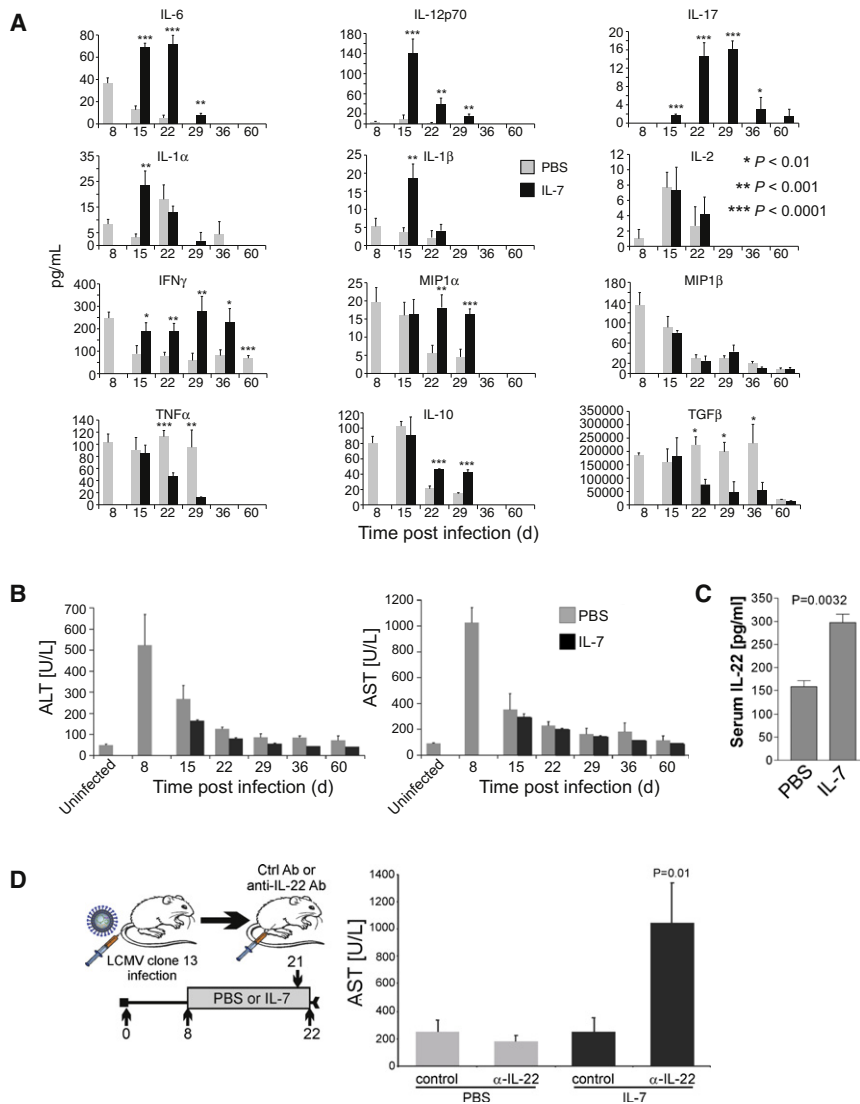


**Figure 5. IL-7 Enhances Cytokine Responses Favoring IL-6, IL-17, and IFN $\gamma$  Production and Promotes IL-22-Mediated Cytoprotection**

(A) Serum cytokine levels in IL-7- and PBS-treated clone 13-infected mice. Graphs represent averages and SD of data collected from 12 mice in each group. This experiment was repeated three times. Asterisks represent p values as indicated.

(B) Serum AST and ALT liver enzyme levels in uninfected and infected mice treated with IL-7 or PBS. Graphs represent averages and SD of data collected from 12 mice in each group.

(C) Serum IL-22 levels in IL-7- and PBS-treated clone 13-infected animals 21 days following infection. Graphs represent averages and SEM of data collected from four mice in each group.

(D) Serum AST levels in infected mice treated with PBS or IL-7 after IL-22 neutralization. Mice were infected with clone 13 and 8 days postinfection treated with IL-7 or PBS. On day 21 postinfection, IL-22-neutralizing mAb was administered, and serum AST levels were determined the following day. Graphs represent averages and SEM of data obtained from four mice in each group. This experiment was repeated twice.

See also Figure S3.

liver pathology, we utilized anti-IL-22 mAb to neutralize the effect of this cytokine. Neutralizing IL-22 caused a significant hepatitis in IL-7-treated clone 13-infected mice (Figure 5D). This cytoprotective effect of IL-22 was not evident in PBS-treated control animals when IL-22 was neutralized (Figure 5D), most likely due to the lack of hepatic infiltration and the poor cytokine response associated with chronically infected PBS treated mice (Figure 1C and Figure 5A). These data indicate that IL-7 is able to

### IL-7 Promotes IL-22-Mediated Cytoprotection during Clone 13 Infection

As a marker of immune-mediated damage and bystander pathology, we examined serum liver enzyme levels. Clone 13 causes a mild hepatitis, with an elevation of both serum aspartate transaminase (AST) and alanine transaminase (ALT) 8 days following infection. Compared to controls, IL-7 did not exacerbate liver disease, which resolved quickly in all animals (Figure 5B). IL-6 has been shown to protect hepatocytes from T cell-mediated injury, and this cytokine is significantly upregulated in IL-7-treated animals (Klein et al., 2005). IL-22 has also been identified as a cytoprotective cytokine that limits hepatotoxicity associated with ConA-induced cytokine storms (Radaeva et al., 2004; Zenewicz et al., 2007). We found a 2-fold increase in serum IL-22 levels in IL-7-treated mice compared to PBS treatment in clone 13-infected animals (Figure 5C). To determine whether the high levels of IL-22 in IL-7-treated clone 13-infected animals was responsible for the lack of significant

limit its potential toxicity, which may be secondary to the augmented cytokine responses, by enhancing IL-22-mediated cytoprotection.

IL-22 is produced by Th17 cells (Zenewicz et al., 2007), lymphoid tissue inducer cells (LTI), and a subset of LTI-like cells in the gut that express the natural cytotoxic receptor Nkp46 (reviewed in Colonna [2009]). To determine which cells were contributing to the increase in IL-22, we first determined whether this cytokine was locally produced in the liver. We found that IL-22 levels were 4-fold higher in the liver than in serum of IL-7-treated clone 13-infected mice (Figure S3A). This indicates that there is an endogenous source of IL-22 production in the liver. Major producers of IL-22 in the liver of IL-7-treated clone 13-infected animals were CD4<sup>+</sup>CD3<sup>+</sup>TCR $\alpha\beta$ <sup>+</sup> T cells (Figure S3B and data not shown). Hence, conventional CD4 T cells, similar to those that secrete IL-17 (Figure S3B), are a significant source of IL-22 in the liver of IL-7-treated clone 13-infected mice.

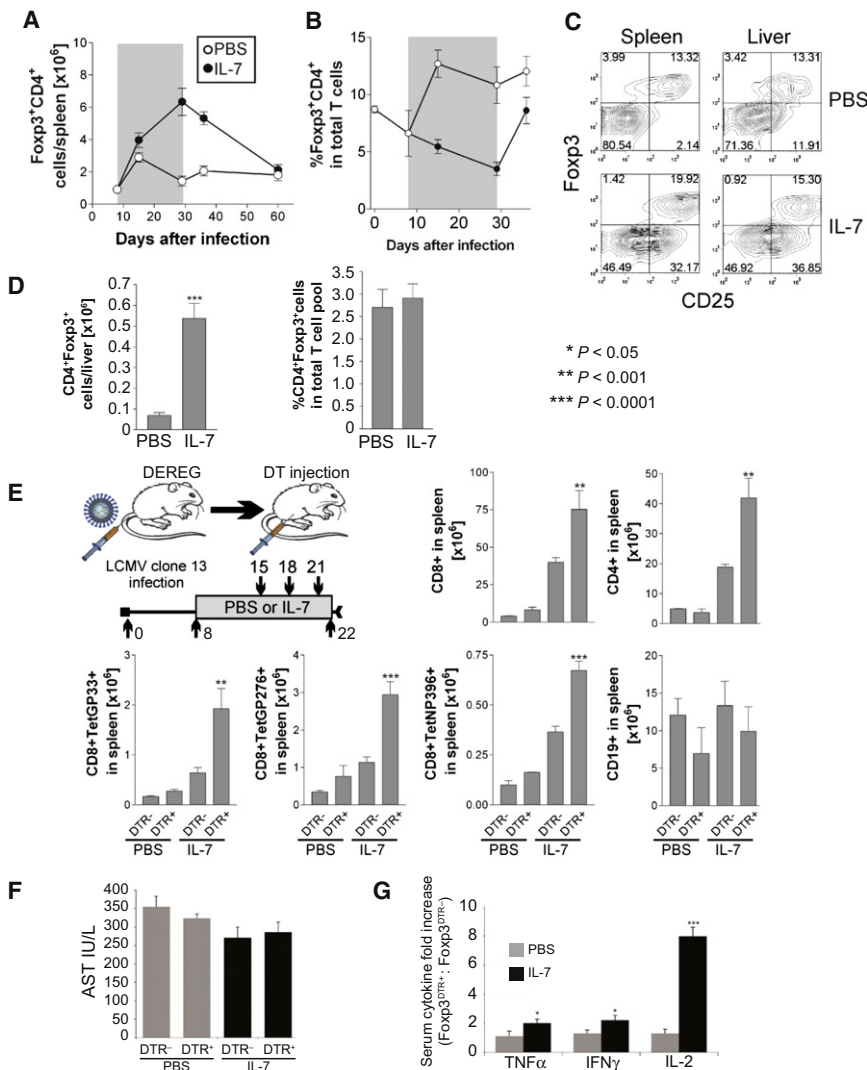


**Figure 6. IL-7 Decreases the Proportion of Treg among the Total T Cell Pool, and Further Depletion of Treg Enhances Some IL-7 Effects**

(A–D) The total number of Treg in spleen (A) and liver (D) and the number of Treg as a proportion of total T cells in spleen (B) and liver (D) are represented as averages and SEM of data obtained from four mice in each group. Liver Treg numbers were determined at day 29 postinfection. This experiment was repeated twice. Typical levels of CD25 expression on Fcpx3<sup>+</sup> Treg and non-Treg CD4 T cells in spleen and liver of PBS- and IL-7-treated clone 13-infected mice at day 29 postinfection are shown (C). These contour plots are representative of more than six analyses performed independently.

(E) Treg were depleted in clone 13-infected animals by injection of DT at the indicated time points. Nontransgenic littermate control (DTR<sup>-</sup>) mice were also injected with DT for comparison. Total lymphocytes and LCMV-specific T cells were quantified in the spleens of PBS- and IL-7-treated animals. Graphs represent averages and SEM of data obtained from four mice in each group. This experiment was repeated twice, and asterisks represent p values as indicated.

(F) Liver enzyme assay in Treg-depleted animals infected with clone 13. AST levels were measured at day 22 postinfection after Treg depletion in clone 13-infected mice treated with PBS or IL-7. Graphs represent averages and SEM of data obtained from four mice in each group. This experiment was repeated twice.

(G) Serum cytokine levels in Treg-depleted animals infected with clone 13. Serum cytokine levels were measured at day 22 postinfection after Treg depletion in clone 13-infected mice treated with PBS or IL-7. Graphs represent averages and SEM of data obtained from four mice in each group. This experiment was repeated twice.

**IL-7 Limits T Regulatory Cell Numbers in Clone 13 Infection**

Reports have suggested that IL-7 renders effector cells refractory to the effects of T regulatory cells (Treg) (Pellegriani et al., 2009; Ruprecht et al., 2005). We investigated the effects of IL-7 on Treg physiology in the setting of chronic clone 13 infection. We found that the absolute number of Treg or Fcpx3<sup>+</sup>CD4<sup>+</sup> T cells was increased in the spleen of IL-7-treated clone 13-infected mice compared to controls. However, when compared to the overall increase in T cell numbers, Treg were dramatically underrepresented in IL-7-treated animals (Figure 6A–6D).

To determine the physiological relevance of Treg in the setting of chronic infection, we utilized BAC-transgenic DEREG mice that express a diphtheria toxin (DT) receptor-GFP fusion protein under the control of the *foxp3* gene locus (Lahl et al., 2007). This allowed us to follow and selectively deplete Fcpx3<sup>+</sup> Treg cells by DT injection. We were able to efficiently delete GFP<sup>+</sup> cells without overt adverse effect on the animals (data not shown).

Clone 13-infected mice treated with PBS did not show any significant differences in absolute T cell numbers or GP- or NP-specific T cell numbers after Treg depletion (Figure 6E). Interestingly, IL-7-treated animals showed a 2- to 3-fold increase in the numbers of CD8-, CD4-, GP-, and NP-specific T cells, whereas B cell numbers were not affected after Treg depletion (Figure 6E). In all animals, the depletion of Treg did not cause short-term immune-mediated pathology, as liver function tests did not become elevated after depletion (Figure 6F). These data suggest that, at least in the short term, Treg do not impede an immune response in chronic clone 13 infection. However, Treg do partially abrogate IL-7's ability to expand T cells, but notably, viral titers in both IL-7- and PBS-treated animals were not altered in the absence of Treg (data not shown). Because previous experiments have shown that IL-7 renders T effector cells refractory to the inhibitory effects of Treg (Pellegriani et al., 2009; Ruprecht et al., 2005), we postulated that the increase in T cell numbers observed only in IL-7-treated animals was perhaps due to the consumption of IL-2 by Treg (Pandiyan

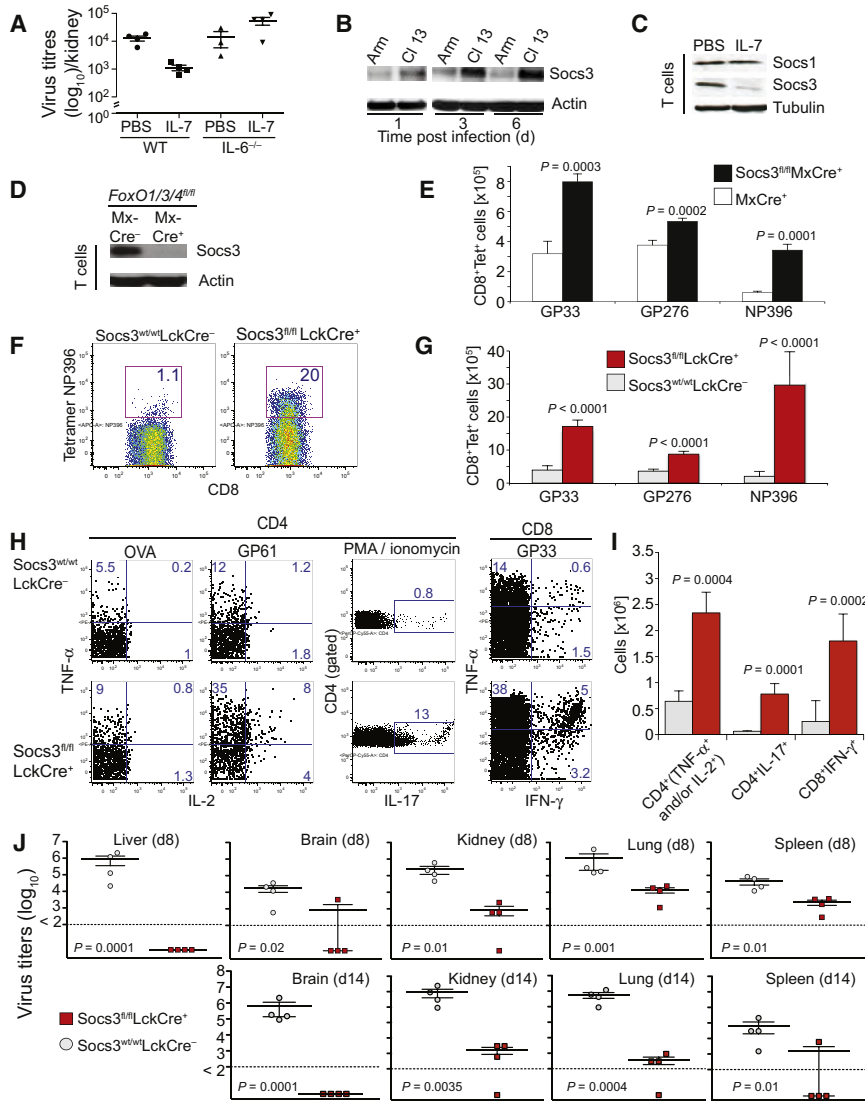


**Figure 7. IL-7 Represses Socs3 Expression in T Cells, and Conditional Deletion of socs3 Potently Augments Antiviral Immunity**

(A) Viral titers performed 3 weeks postinfection in IL-6-deficient and control mice treated with PBS or IL-7 for 2 weeks starting 8 days after infection. Error bars represent SEM.

(B) Socs3 expression in T cells from LCMV Armstrong and LCMV clone 13-infected animals. Socs3 protein levels in sorted T cells were determined by western blot at the indicated time points after infection.

(C) Expression of Socs3 in splenic T cells from infected mice treated with IL-7 or PBS in vivo for 5 days. Direct ex vivo western blot analysis was performed for Socs1 and Socs3 levels. Blots are representative of three independent experiments.

(D) Socs3 expression levels determined by western blot in naive T cells isolated from FoxO1/3/4 conditionally deficient mice or control animals.

(E) Numbers of LCMV clone 13-specific CD8 T cells in control and Socs3 conditionally (MxCre) deleted mice 6 days post-LCMV clone 13 infection. Error bars represent SD.

(F) Dot plots showing proportions of NP396-specific CD8 T cells in Socs3 conditionally (LckCre) deleted mice and control mice 8 days after infection.

(G) Numbers of LCMV clone 13-specific CD8 T cells in control and Socs3 conditionally (Lck) deleted mice 8 days post-LCMV clone 13 infection. Error bars represent SD.

(H) Ex vivo cytokine production by LCMV clone 13-specific T cells from indicated mice at day 8 postinfection. Splenocytes were restimulated in vitro with control (OVA) or cognate (GP61) peptides to quantify CD4 T cells and GP33 to quantify CD8 T cells. Phorbol myristate acetate (PMA) and ionomycin restimulation were used for the quantification of IL-17-producing CD4 T cells. Proportions in each quadrant are indicated.

(I) Average numbers of T cells secreting indicated cytokines in aforementioned assay. Errors bars represent SD.

(J) Virus titers in the indicated mice and organs on day 8 (top) and day 14 (bottom) postinfection.

See also Figure S4 and Figure S5.

et al., 2007). In the absence of Treg, the abundance of this cytokine may further augment the expanded immune response seen in IL-7-treated animals. Indeed, when we examined the level of IL-2 compared to other cytokines, it was proportionally increased in IL-7-treated and Treg-depleted animals compared to nondepleted animals. This consumption of IL-2 in IL-7-treated animals is further supported by the high level of CD25 expression on both Treg and non-Treg CD4 T cell populations at day 29 postinfection (Figure 6C). Our data therefore suggest that depletion of Treg may complement the effects of IL-7 by removing a potential cytokine sink.

### IL-7 Reprograms T Cells to Repress Socs3 Inhibitory Pathways

In view of the dramatic increase in numerous cytokine levels and the ability of IL-7-treated mice to efficiently clear virus, we

investigated whether inhibitors of cytokine signaling may be repressed. We focused on Socs3, given its prominent role in the negative regulation of IL-6 signaling (Croker et al., 2003; Lang et al., 2003) and prominent increase of this cytokine in the context of IL-7 treatment. Interestingly, the efficacy of IL-7 in promoting cytokine responses, including IL-22 and T cell expansion and viral clearance, is diminished in IL-6-deficient mice (Figure 7A and Figures S4A–S4C). Furthermore, it has been shown that, in the absence of Socs3, IL-6 signaling is reprogrammed to mimic IFN responses, and this may contribute to more efficient viral elimination (Croker et al., 2003; Lang et al., 2003). We first investigated whether Socs3 levels in T cells are aberrantly upregulated in clone 13 infection compared to acute LCMV Armstrong infection. Even at very early time points during clone 13 infection, the levels of Socs3 in T cells, purified and analyzed directly ex vivo, were substantially higher

in clone 13-infected mice compared to Armstrong infected animals (Figure 7B). We then purified total T cells from PBS- or IL-7-treated clone 13-infected animals. Direct ex vivo western blot analysis was performed and established that IL-7 treatment resulted in a substantial reduction in Socs3 levels in T cells (Figure 7C). We did not observe any differences in Socs1 levels. These data elucidate a pathway downstream of IL-7 that interferes with Socs3 inhibition of cytokine-mediated signaling.

### Socs3 Is Endogenously Regulated by FoxO Transcription Factors

It is generally accepted that Socs3 is induced with cytokine signaling via a Stat-dependent pathway. It is unusual then that IL-7, a potent inducer of Stat5 signaling, is able to repress Socs3. However, FoxO transcription factors can be negatively regulated by IL-7 and perhaps other cytokines that signal via the common  $\gamma$  chain receptor (reviewed in Kittipatarin and Khaled [2007]), and under certain circumstances, Stat5 transcriptional activity may negatively regulate FoxO1 (Stittrich et al., 2010). Therefore, we tested whether FoxO transcription factors are involved in Socs3 induction. Mice that had all six alleles of *foxO* conditionally targeted (*foxO1/3/4*) were crossed to MxCre transgenic mice to generate (*foxO1/3/4*)<sup>fl/fl</sup>MxCre animals. These mice were injected with poly I:C to generate animals that were deficient in FoxO1/3/4 in the hemopoietic compartment (Paik et al., 2007). T cells were purified from these animals well before the development of any malignancies or abnormalities. T cells isolated from animals deficient in FoxO transcription factors had dramatically reduced levels of Socs3, as determined by western blot (Figure 7D). Collectively, these data indicate that IL-7 may repress Socs3 expression via inhibition of FoxO transcriptional activity.

### Mice Conditionally Deficient in Socs3 Mimic the IL-7-Induced T Cell Phenotype in Clone 13-Infected Animals

To assess whether a deficiency in Socs3 in T cells could replicate some of the IL-7-induced effects that we observed in clone 13-infected animals, we used mice that had *socs3* conditionally targeted (Crocker et al., 2003). These *socs3*<sup>fl/fl</sup> mice were crossed with MxCre transgenic mice, and gene deletion throughout the hemopoietic compartment was induced by clone 13 infection, which induces a type I IFN response and activation of the IFN-responsive Mx1 promoter. Ex vivo analysis by PCR confirmed that *socs3* was deleted in purified peripheral T cells by day 3 postinfection (data not shown). By day 6 postinfection, all mice had to be euthanized due to severe illness. At this time point, Socs3<sup>fl/fl</sup>MxCre<sup>+</sup> mice had a 2.5-fold increase in the number of splenic GP33-specific CD8 T cells and a 6-fold increase in the number of NP396-specific CD8 T cells compared to control animals (Figure 7E). Ex vivo analysis of Socs3<sup>fl/fl</sup>MxCre<sup>+</sup> GP33-specific CD8 T cells at day 6 postinfection demonstrated a 5.5-fold increase in the ability of these cells to secrete both IFN- $\gamma$  and TNF- $\alpha$  compared to controls (Figure S5A). Clone 13-infected Socs3<sup>fl/fl</sup>MxCre<sup>+</sup> mice had a dramatic neutrophilia with a 3.5-fold increase in the number of splenic granulocytes (Figure S5B). This substantial neutrophilia, which is likely due to Socs3 deficiency in granulocytes induced by clone 13 infec-

tion, may explain the illness that the mice succumb to. Liver function tests indicated a prominent hepatitis in clone 13-infected Socs3<sup>fl/fl</sup>MxCre<sup>+</sup> mice compared to controls (Figure S5C). The exact cause of lethality in clone 13-infected Socs3<sup>fl/fl</sup>MxCre<sup>+</sup> is not clear but likely relates to the severe granulocytosis observed in these animals. To avoid the development of granulocytosis and early lethality, we next used Socs3<sup>fl/fl</sup>LckCre<sup>+</sup> mice to specifically delete *socs3* in T cells.

### T Cell-Specific Deletion of *socs3* Augments Immunity to Efficiently Eliminate Virus

Analysis of Socs3<sup>fl/fl</sup>LckCre<sup>+</sup> mice on day 8 post-LCMV clone 13 infection showed a profound augmentation of immunity, with a 15-fold increase in the number of NP396 virus-specific CD8 T cells compared to controls (Figures 7F and 7G). These mice did not develop a granulocytosis postinfection (Figure S5D) and showed no signs of increased collateral liver pathology (Figure S5C), morbidity, or mortality compared to control animals. Ex vivo analysis of T cells from Socs3<sup>fl/fl</sup>LckCre<sup>+</sup>-infected mice at day 8 postinfection showed a 4-fold increase in the ability of virus-specific CD4 T cells to secrete TNF- $\alpha$  and/or IL-2, a 7-fold increase in the ability of virus-specific CD8 T cells to secrete IFN- $\gamma$ , and a 17-fold increase in the number of Th17 cells (Figures 7H and 7I). The severe granulocytosis and early mortality in LCMV clone 13-infected Socs3<sup>fl/fl</sup>MxCre<sup>+</sup> mice prevented the elimination of virus, but Socs3<sup>fl/fl</sup>LckCre<sup>+</sup> LCMV-infected mice progressively and efficiently cleared virus from organs with no mortality (Figure S5E, Figure 7J, and data not shown). Consistent with viral clearance, we observed a contraction of the immune response at day 14 postinfection in Socs3<sup>fl/fl</sup>LckCre<sup>+</sup> mice (Figures S5F and S5G). However, a 3-fold increase in the number of residual high-affinity NP396 virus-specific CD8 T cells persisted in Socs3<sup>fl/fl</sup>LckCre<sup>+</sup> mice compared to controls at day 14 postinfection (Figure S5G). These data indicate that the T cell-intrinsic Socs3 induction is a major factor contributing to immunological failure in the setting of chronic active infection.

## DISCUSSION

Utilizing the clone 13 model, we have shown that IL-7 is able to overcome many of the factors that thwart an effective immune response during chronic overwhelming viremia. One host inhibitory pathway that may restrict immune responses involves the Socs family of proteins that critically regulate cytokine signaling. Socs3 has been identified as the major regulatory molecule that dampens IL-6 signaling (Yoshimura et al., 2007). Indeed, studies have shown that the pattern of gene expression induced by IL-6 in Socs3-deficient animals mimics that induced by IFN- $\gamma$  (Crocker et al., 2003; Lang et al., 2003). We have shown that IL-7 is able to downregulate Socs3 levels in T cells, and additionally, it promotes IL-6 production. Together, this would reprogram cells to promote an IFN-like response and facilitate viral clearance. Furthermore, Socs3 has recently been reported to function as an intrinsic negative regulator of T cell proliferation (Brender et al., 2007). Thus, by repressing Socs3, IL-7 may promote innate antiviral mechanisms and also promote expansion and function of the adaptive immune response.

We found that T cells in clone 13-infected mice have much higher levels of Socs3 protein compared to T cells from LCMV Armstrong-infected animals. The importance of both IL-6 and Socs3 repression in mediating the therapeutic potential of IL-7 was evidenced by the reduced efficacy of IL-7 therapy in IL-6-deficient animals. We were able to delete *socs3* throughout the hemopoietic compartment of gene-targeted mice contemporaneously with clone 13 infection to avoid potential developmental confounders and found that many of the effects that we observed with IL-7 therapy were replicated in this system. The MxCre transgene was useful in our studies to coincide the deletion of *socs3* with the time of infection, but the neutrophilia associated with broad deletion of *socs3* across the hematopoietic lineage was associated with early lethality. This adverse event requires further investigation in the future. Notably, IL-7 does not induce a granulocytosis, as its effects are limited to cells that express IL-7R, and hence its ability to repress Socs3 would be restricted to T cells and perhaps other immune cell subsets, but not neutrophils. We observed a dramatic increase in LCMV clone 13-specific immune responses and viral clearance in mice lacking Socs3 just in T cells. Importantly, these mice showed no signs of increased collateral damage or pathology compared to controls. The ability of IL-7 to repress Socs3 in T cells and perhaps other IL-7 responsive cells has significant implications for its use in manipulating innate and adaptive responses to favor elimination of pathogens.

Despite the large increase in cytokine levels and the marked infiltration of lymphocytes in organs of clone 13-infected animals receiving IL-7 therapy, we found no significant indication of bystander hepatitis. We have shown that IL-7 favors *in vivo* Th17 differentiation with IL-17 production. This may be due to IL-7-induced repression of Socs3 and promotion of an IL-17-IL-6 feedback loop (Ogura et al., 2008). Th17 and other cells have been identified as a major source of IL-22 (Colonna, 2009; Ouyang et al., 2008), which is critically important in protecting hepatocytes and perhaps other cells from immune-mediated bystander damage (Aujla et al., 2008; Laurence et al., 2008; Radaeva et al., 2004; Sugimoto et al., 2008; Zenewicz et al., 2007; Zheng et al., 2008). Indeed, in our clone 13 model, we found that IL-7 promotes IL-22 production, and this mitigates collateral liver damage. These findings are particularly pertinent to the use of IL-7 in chronic viral hepatitis. In HIV infection, IL-7 also holds much promise. Systemic immune activation is a hallmark of HIV disease that has been attributed to circulating microbial products, which may be a consequence of bacterial translocation across damaged gut mucosa (Brenchley et al., 2006). Endogenous production of IL-22 has been shown to protect mucosal sites (Aujla et al., 2008; Sugimoto et al., 2008; Zheng et al., 2008).

Another limitation of the immune system in HIV infection is the inability to replete peripheral losses due to attrition of T lymphocytes caused by the virus itself or by secondary effects due to the high level of viremia (Chase et al., 2006). During clone 13 infection, this is most apparent with the deletion of NP396-specific T cell clones. IL-7 significantly increased the number of these clones, but there was also a more general increase in non-LCMV-specific CD4 and CD8 T cells. Additionally, IL-7 promoted thymic output and substantially expanded the naive T cell pool in infected mice.

Our data provide insights into the inhibitory pathways that function to impede immune responses in chronic infection. We elucidate a molecular mechanism whereby IL-7 is able to repress Socs3 levels in immune cells to promote extensive expansion of naive and effector T cells. Furthermore, we highlight the attributes of IL-7 in augmenting recent thymic emigrants in the face of persistent infection and its ability to promote IL-22 production and hence limit bystander cytotoxicity. Our data suggest that IL-7 therapy may be a useful adjuvant in chronic viral diseases like HIV. Antiretroviral therapy is successful in reducing viral loads to undetectable levels, and in this setting, T cells become more responsive to IL-7 through the restoration of IL-7R, thereby enabling their rescue. In this context of reduced viral load, IL-7 therapy can be used to produce and expand specific T cells and promote a broad and durable immune-mediated antiviral response. Furthermore, the secondary cytoprotective effects of IL-7 have therapeutic implications for the management of hepatitis C virus infections.

## EXPERIMENTAL PROCEDURES

### Mice and Viral Infection

The source and/or derivation of mice and viruses is detailed in the [Extended Experimental Procedures](#). Infection was initiated by injecting  $2 \times 10^6$  PFU LCMV clone 13 into the tail vein of 4 to 5-week-old mice. Institutional Animal Ethics and Care Committees at the Princess Margaret Hospital and the Walter and Eliza Hall Institute approved all experiments. Procedures complied with Institutional Animal Care regulations, as detailed in the [Extended Experimental Procedures](#).

### IL-7 Treatment

Eight days after infection, mice were injected subcutaneously once daily with 10  $\mu$ g of recombinant human IL-7 or PBS for 3 weeks. Recombinant CHO cell-derived human IL-7 was provided by Cytheris Inc. (Issy les Moulineaux, France).

### Histology and Flow Cytometry

Immunohistological staining has been previously described (Nguyen et al., 2002). Detailed protocols for the isolation, staining, and *in vitro* restimulation of lymphocytes are provided in the [Extended Experimental Procedures](#).

### Viral Titer Assays

Organs were homogenized using the QIAGEN TissueLyser, and viral titers were quantified by focus-forming assays using MC57 fibroblast cells, as previously described (Battegay et al., 1991).

### Analysis of Transgenic RAG-GFP Mice

Transgenic animals were infected with clone 13 and treated with IL-7 or PBS 8 days after infection, as described above. After 5 days of treatment, thymic and splenic T cells were isolated, stained, and analyzed for GFP expression by flow cytometry.

### Serum Cytokine Assays

Serum cytokine levels were assayed using the SearchLight Array (Pierce Biotechnology, Woburn, MA). IL-22 was measured using a quantikine immunoassay kit (R&D Systems).

### Cell Depletion and Cytokine Neutralization

Detailed protocols for cell depletion, including Treg depletion, and IL-22 *in vivo* neutralization are provided in the [Extended Experimental Procedures](#).

### Liver Enzyme Assays

Serum was analyzed for AST and ALT levels (Vita-Tech Canada).

### Western Blots

Direct ex vivo analysis of protein expression levels in specific cell populations is described in the [Extended Experimental Procedures](#).

### Statistical Analysis

Animal cohorts used in treatment arms were designed to contain an equal distribution of sexes. An unpaired two-tailed Student's *t* test was used to determine the statistical significance of observed differences between groups. Data were analyzed as continuous variables with a normal distribution. A time to event analysis and log-rank tests were performed on viral clearance kinetics. Analysis of variance was used for comparisons involving more than two groups.

### SUPPLEMENTAL INFORMATION

Supplemental Information includes Extended Experimental Procedures and five figures and can be found with this article online at [doi:10.1016/j.cell.2011.01.011](https://doi.org/10.1016/j.cell.2011.01.011).

### ACKNOWLEDGMENTS

Dr. Mandana Nikpour assisted with statistical analyses. Marina Zaitseva contributed to the analysis of thymic emigrants; Alain Lamarre, Paul Jolicoeur, and Michel Nussenzweig provided reagents and mice. This work was supported by a Canadian Institute for Health Research grant to T.W.M. and P.S.O. (CIHR-MOP-106529) and a Terry Fox Cancer Foundation National Cancer Institute of Canada grant to T.W.M. T.C. was supported by the Boninchi Foundation (Geneva, Switzerland) and The Terry Fox Foundation through an award from the National Cancer Institute of Canada. M.P. was supported through an Irvington Institute Fellowship with the Cancer Research Institute (New York, NY) and an Australian National Health and Medical Research Council Fellowship. S.B. receives support from the Natural Sciences and Engineering Research Council of Canada. P.S.O. holds a Canada Research Chair in autoimmunity and tumor immunity. This research was also funded, in part, by the Ontario Ministry of Health and Long Term Care (OMOHLTC). The views expressed do not necessarily reflect those of the OMOHLTC.

M.P., T.C., J.G.T., S.P.P., A.E.L., A.R.E., A.S., P.A.L., J.-h.P., S.B., P.S.O., and T.W.M. designed and performed all of the research with technical assistance and advice from K.S.L., T.S., T.F.T., J.-h.P., and R.A.D. TWINCOER is a joint venture between the Helmholtz Centre for Infection Research (HZI) Braunschweig and the Hannover Medical School (MHH). These authors have no competing financial interests and conducted the experiments and analyzed data independently from Cytheris Inc. M.M. and B.A. provided advice and technical information. M.M. is the founder and Chief Executive Officer and B.A. is an employee of Cytheris Inc.; both have financial interest in its capital.

Received: March 30, 2009

Revised: November 8, 2010

Accepted: December 17, 2010

Published online: February 3, 2011

### REFERENCES

- Aujla, S.J., Chan, Y.R., Zheng, M., Fei, M., Askew, D.J., Pociask, D.A., Reinhart, T.A., McAllister, F., Edeal, J., Gaus, K., et al. (2008). IL-22 mediates mucosal host defense against Gram-negative bacterial pneumonia. *Nat. Med.* **14**, 275–281.
- Barber, D.L., Wherry, E.J., Masopust, D., Zhu, B., Allison, J.P., Sharpe, A.H., Freeman, G.J., and Ahmed, R. (2006). Restoring function in exhausted CD8 T cells during chronic viral infection. *Nature* **439**, 682–687.
- Battegay, M., Cooper, S., Althage, A., Bänziger, J., Hengartner, H., and Zinkernagel, R.M. (1991). Quantification of lymphocytic choriomeningitis virus with an immunological focus assay in 24- or 96-well plates. *J. Virol. Methods* **33**, 191–198.
- Beq, S., Nugeyre, M.T., Ho Tsong Fang, R., Gautier, D., Legrand, R., Schmitt, N., Estaquier, J., Barré-Sinoussi, F., Hurtrel, B., Cheyrier, R., and Israël, N. (2006). IL-7 induces immunological improvement in SIV-infected rhesus macaques under antiviral therapy. *J. Immunol.* **176**, 914–922.
- Bouaziz, J.D., Yanaba, K., Venturi, G.M., Wang, Y., Tisch, R.M., Poe, J.C., and Tedder, T.F. (2007). Therapeutic B cell depletion impairs adaptive and autoreactive CD4+ T cell activation in mice. *Proc. Natl. Acad. Sci. USA* **104**, 20878–20883.
- Brenchley, J.M., Price, D.A., Schacker, T.W., Asher, T.E., Silvestri, G., Rao, S., Kazzaz, Z., Bornstein, E., Lambotte, O., Altmann, D., et al. (2006). Microbial translocation is a cause of systemic immune activation in chronic HIV infection. *Nat. Med.* **12**, 1365–1371.
- Brender, C., Tannahill, G.M., Jenkins, B.J., Fletcher, J., Columbus, R., Saris, C.J., Ernst, M., Nicola, N.A., Hilton, D.J., Alexander, W.S., and Starr, R. (2007). Suppressor of cytokine signaling 3 regulates CD8 T-cell proliferation by inhibition of interleukins 6 and 27. *Blood* **110**, 2528–2536.
- Brooks, D.G., Trifilo, M.J., Edelman, K.H., Teyton, L., McGavern, D.B., and Oldstone, M.B. (2006). Interleukin-10 determines viral clearance or persistence in vivo. *Nat. Med.* **12**, 1301–1309.
- Chase, A., Zhou, Y., and Siliciano, R.F. (2006). HIV-1-induced depletion of CD4+ T cells in the gut: mechanism and therapeutic implications. *Trends Pharmacol. Sci.* **27**, 4–7.
- Chu, Y.W., Memon, S.A., Sharrow, S.O., Hakim, F.T., Eckhaus, M., Lucas, P.J., and Gress, R.E. (2004). Exogenous IL-7 increases recent thymic emigrants in peripheral lymphoid tissue without enhanced thymic function. *Blood* **104**, 1110–1119.
- Colonna, M. (2009). Interleukin-22-producing natural killer cells and lymphoid tissue inducer-like cells in mucosal immunity. *Immunity* **31**, 15–23.
- Croker, B.A., Krebs, D.L., Zhang, J.G., Wormald, S., Willson, T.A., Stanley, E.G., Robb, L., Greenhalgh, C.J., Förster, I., Clausen, B.E., et al. (2003). SOCS3 negatively regulates IL-6 signaling in vivo. *Nat. Immunol.* **4**, 540–545.
- Day, C.L., Kaufmann, D.E., Kiepiela, P., Brown, J.A., Moodley, E.S., Reddy, S., Mackey, E.W., Miller, J.D., Leslie, A.J., DePierres, C., et al. (2006). PD-1 expression on HIV-specific T cells is associated with T-cell exhaustion and disease progression. *Nature* **443**, 350–354.
- Ejmaes, M., Filippi, C.M., Martinic, M.M., Ling, E.M., Togher, L.M., Crotty, S., and von Herrath, M.G. (2006). Resolution of a chronic viral infection after interleukin-10 receptor blockade. *J. Exp. Med.* **203**, 2461–2472.
- Fry, T.J., Moniuszko, M., Creekmore, S., Donohue, S.J., Douek, D.C., Gardina, S., Hecht, T.T., Hill, B.J., Komschlies, K., Tomaszewski, J., et al. (2003). IL-7 therapy dramatically alters peripheral T-cell homeostasis in normal and SIV-infected nonhuman primates. *Blood* **101**, 2294–2299.
- Kittipatarin, C., and Khaled, A.R. (2007). Interlinking interleukin-7. *Cytokine* **39**, 75–83.
- Klein, C., Wüstefeld, T., Assmus, U., Roskams, T., Rose-John, S., Müller, M., Manns, M.P., Ernst, M., and Trautwein, C. (2005). The IL-6-gp130-STAT3 pathway in hepatocytes triggers liver protection in T cell-mediated liver injury. *J. Clin. Invest.* **115**, 860–869.
- Klenerman, P., and Hill, A. (2005). T cells and viral persistence: lessons from diverse infections. *Nat. Immunol.* **6**, 873–879.
- Lahl, K., Loddenkemper, C., Drouin, C., Freyer, J., Arnason, J., Eberl, G., Hamann, A., Wagner, H., Huehn, J., and Sparwasser, T. (2007). Selective depletion of Foxp3+ regulatory T cells induces a scurfy-like disease. *J. Exp. Med.* **204**, 57–63.
- Lang, R., Pauleau, A.L., Parganas, E., Takahashi, Y., Mages, J., Ihle, J.N., Rutschman, R., and Murray, P.J. (2003). SOCS3 regulates the plasticity of gp130 signaling. *Nat. Immunol.* **4**, 546–550.
- Laurence, A., O'Shea, J.J., and Watford, W.T. (2008). Interleukin-22: a sheep in wolf's clothing. *Nat. Med.* **14**, 247–249.
- Levy, Y., Lacabaratz, C., Weiss, L., Viard, J.P., Goujard, C., Lelièvre, J.D., Boué, F., Molina, J.M., Rouzioux, C., Avettand-Fénoël, V., et al. (2009). Enhanced T cell recovery in HIV-1-infected adults through IL-7 treatment. *J. Clin. Invest.* **119**, 997–1007.
- Li, Q., Duan, L., Estes, J.D., Ma, Z.M., Rourke, T., Wang, Y., Reilly, C., Carlis, J., Miller, C.J., and Haase, A.T. (2005). Peak SIV replication in resting memory

- CD4+ T cells depletes gut lamina propria CD4+ T cells. *Nature* 434, 1148–1152.
- Mattapallil, J.J., Douek, D.C., Hill, B., Nishimura, Y., Martin, M., and Roederer, M. (2005). Massive infection and loss of memory CD4+ T cells in multiple tissues during acute SIV infection. *Nature* 434, 1093–1097.
- Matter, M., Odermatt, B., Yagita, H., Nuoffer, J.M., and Ochsenbein, A.F. (2006). Elimination of chronic viral infection by blocking CD27 signaling. *J. Exp. Med.* 203, 2145–2155.
- Nguyen, L.T., Elford, A.R., Murakami, K., Garza, K.M., Schoenberger, S.P., Odermatt, B., Speiser, D.E., and Ohashi, P.S. (2002). Tumor growth enhances cross-presentation leading to limited T cell activation without tolerance. *J. Exp. Med.* 195, 423–435.
- Nugeyre, M.T., Monceaux, V., Beq, S., Cumont, M.C., Ho Tsong Fang, R., Chène, L., Morre, M., Barré-Sinoussi, F., Hurtrel, B., and Israël, N. (2003). IL-7 stimulates T cell renewal without increasing viral replication in simian immunodeficiency virus-infected macaques. *J. Immunol.* 171, 4447–4453.
- Ogura, H., Murakami, M., Okuyama, Y., Tsuruoka, M., Kitabayashi, C., Kanamoto, M., Nishihara, M., Iwakura, Y., and Hirano, T. (2008). Interleukin-17 promotes autoimmunity by triggering a positive-feedback loop via interleukin-6 induction. *Immunity* 29, 628–636.
- Ouyang, W., Kolls, J.K., and Zheng, Y. (2008). The biological functions of T helper 17 cell effector cytokines in inflammation. *Immunity* 28, 454–467.
- Paik, J.H., Kollipara, R., Chu, G., Ji, H., Xiao, Y., Ding, Z., Miao, L., Tothova, Z., Horner, J.W., Carrasco, D.R., et al. (2007). FoxOs are lineage-restricted redundant tumor suppressors and regulate endothelial cell homeostasis. *Cell* 128, 309–323.
- Pandiyani, P., Zheng, L., Ishihara, S., Reed, J., and Lenardo, M.J. (2007). CD4+CD25+Foxp3+ regulatory T cells induce cytokine deprivation-mediated apoptosis of effector CD4+ T cells. *Nat. Immunol.* 8, 1353–1362.
- Pellegrini, M., Calzascia, T., Elford, A.R., Shahinian, A., Lin, A.E., Dissanayake, D., Dhanji, S., Nguyen, L.T., Gronski, M.A., Morre, M., et al. (2009). Adjuvant IL-7 antagonizes multiple cellular and molecular inhibitory networks to enhance immunotherapies. *Nat. Med.* 15, 528–536.
- Radaeva, S., Sun, R., Pan, H.N., Hong, F., and Gao, B. (2004). Interleukin 22 (IL-22) plays a protective role in T cell-mediated murine hepatitis: IL-22 is a survival factor for hepatocytes via STAT3 activation. *Hepatology* 39, 1332–1342.
- Rosenberg, S.A., Sportès, C., Ahmadzadeh, M., Fry, T.J., Ngo, L.T., Schwarz, S.L., Stetler-Stevenson, M., Morton, K.E., Mavroukakis, S.A., Morre, M., et al. (2006). IL-7 administration to humans leads to expansion of CD8+ and CD4+ cells but a relative decrease of CD4+ T-regulatory cells. *J. Immunother.* 29, 313–319.
- Ruprecht, C.R., Gattorno, M., Ferlito, F., Gregorio, A., Martini, A., Lanzavecchia, A., and Sallusto, F. (2005). Coexpression of CD25 and CD27 identifies FoxP3+ regulatory T cells in inflamed synovia. *J. Exp. Med.* 201, 1793–1803.
- Sereti, I., Dunham, R.M., Spritzler, J., Aga, E., Proschan, M.A., Medvik, K., Battaglia, C.A., Landay, A.L., Pahwa, S., Fischl, M.A., et al; ACTG 5214 Study Team. (2009). IL-7 administration drives T cell-cycle entry and expansion in HIV-1 infection. *Blood* 113, 6304–6314.
- Sportès, C., Hakim, F.T., Memon, S.A., Zhang, H., Chua, K.S., Brown, M.R., Fleisher, T.A., Krumlauf, M.C., Babb, R.R., Chow, C.K., et al. (2008). Administration of rhIL-7 in humans increases in vivo TCR repertoire diversity by preferential expansion of naive T cell subsets. *J. Exp. Med.* 205, 1701–1714.
- Stittrich, A.B., Haftmann, C., Sgouroudis, E., Köhl, A.A., Hegazy, A.N., Panse, I., Riedel, R., Flossdorf, M., Dong, J., Fuhrmann, F., et al. (2010). The microRNA miR-182 is induced by IL-2 and promotes clonal expansion of activated helper T lymphocytes. *Nat. Immunol.* 11, 1057–1062.
- Sugimoto, K., Ogawa, A., Mizoguchi, E., Shimomura, Y., Andoh, A., Bhan, A.K., Blumberg, R.S., Xavier, R.J., and Mizoguchi, A. (2008). IL-22 ameliorates intestinal inflammation in a mouse model of ulcerative colitis. *J. Clin. Invest.* 118, 534–544.
- Uchida, J., Hamaguchi, Y., Oliver, J.A., Ravetch, J.V., Poe, J.C., Haas, K.M., and Tedder, T.F. (2004). The innate mononuclear phagocyte network depletes B lymphocytes through Fc receptor-dependent mechanisms during anti-CD20 antibody immunotherapy. *J. Exp. Med.* 199, 1659–1669.
- Wherry, E.J., Blattman, J.N., Murali-Krishna, K., van der Most, R., and Ahmed, R. (2003). Viral persistence alters CD8 T-cell immunodominance and tissue distribution and results in distinct stages of functional impairment. *J. Virol.* 77, 4911–4927.
- Wilson, E.B., and Brooks, D.G. (2010). Translating insights from persistent LCMV infection into anti-HIV immunity. *Immunol. Res.* 48, 3–13.
- Yannoutsos, N., Wilson, P., Yu, W., Chen, H.T., Nussenzweig, A., Petrie, H., and Nussenzweig, M.C. (2001). The role of recombination activating gene (RAG) reinduction in thymocyte development in vivo. *J. Exp. Med.* 194, 471–480.
- Yoshimura, A., Naka, T., and Kubo, M. (2007). SOCS proteins, cytokine signaling and immune regulation. *Nat. Rev. Immunol.* 7, 454–465.
- Yu, W., Nagaoka, H., Jankovic, M., Misulovin, Z., Suh, H., Rolink, A., Melchers, F., Meffre, E., and Nussenzweig, M.C. (1999). Continued RAG expression in late stages of B cell development and no apparent re-induction after immunization. *Nature* 400, 682–687.
- Zenewicz, L.A., Yancopoulos, G.D., Valenzuela, D.M., Murphy, A.J., Karow, M., and Flavell, R.A. (2007). Interleukin-22 but not interleukin-17 provides protection to hepatocytes during acute liver inflammation. *Immunity* 27, 647–659.
- Zheng, Y., Valdez, P.A., Danilenko, D.M., Hu, Y., Sa, S.M., Gong, Q., Abbas, A.R., Modrusan, Z., Ghilardi, N., de Sauvage, F.J., and Ouyang, W. (2008). Interleukin-22 mediates early host defense against attaching and effacing bacterial pathogens. *Nat. Med.* 14, 282–289.
- Zhou, L., Lopes, J.E., Chong, M.M., Ivanov, I.I., Min, R., Vitorica, G.D., Shen, Y., Du, J., Rubtsov, Y.P., Rudensky, A.Y., et al. (2008). TGF-beta-induced Foxp3 inhibits T(H)17 cell differentiation by antagonizing RORgamma function. *Nature* 453, 236–240.

# Structure of the measles virus hemagglutinin bound to its cellular receptor SLAM

Takao Hashiguchi<sup>1</sup>, Toyoyuki Ose<sup>2</sup>, Marie Kubota<sup>1</sup>, Nobuo Maita<sup>3,4</sup>, Jun Kamishikiryo<sup>3</sup>, Katsumi Maenaka<sup>2,3,5</sup> & Yusuke Yanagi<sup>1</sup>

Measles virus, a major cause of childhood morbidity and mortality worldwide, predominantly infects immune cells using signaling lymphocyte activation molecule (SLAM) as a cellular receptor. Here we present crystal structures of measles virus hemagglutinin (MV-H), the receptor-binding glycoprotein, in complex with SLAM. The MV-H head domain binds to a  $\beta$ -sheet of the membrane-distal ectodomain of SLAM using the side of its  $\beta$ -propeller fold. This is distinct from attachment proteins of other paramyxoviruses that bind receptors using the top of their  $\beta$ -propeller. The structure provides templates for antiviral drug design, an explanation for the effectiveness of the measles virus vaccine, and a model of the homophilic SLAM-SLAM interaction involved in immune modulations. Notably, the crystal structures obtained show two forms of the MV-H-SLAM tetrameric assembly (dimer of dimers), which may have implications for the mechanism of fusion triggering.

Measles still causes 4% of all deaths in children under age 5 worldwide, despite the availability of an effective live vaccine and the great efforts made to deliver vaccine to children throughout the world<sup>1,2</sup>. Outbreaks continue to occur, even in industrialized nations when vaccination coverage is low<sup>2</sup>. Measles virus is an enveloped virus with a nonsegmented, negative-strand RNA genome, and is classified as a member of the family Paramyxoviridae<sup>3</sup>. To enter a cell, enveloped viruses must bind to their receptors on host cells and induce fusion of the viral membrane with the host cell membrane<sup>4</sup>. Paramyxoviruses attach to and fuse with host membranes at the cell surface, using two distinct envelope proteins. Of these, the attachment protein is responsible for receptor binding whereas the fusion protein mediates membrane fusion<sup>5</sup>. The mechanism by which receptor binding leads to fusion is not well understood<sup>5-8</sup>. The attachment protein could undergo a conformational change upon binding to receptor. This conformational change would destabilize the metastable fusion protein, causing its refolding, which in turn would drive membrane fusion. Alternatively, the attachment protein could serve as a clamp that stabilizes the fusion protein in its prefusion state. Receptor binding of the attachment protein would release the fusion protein from the clamp to facilitate its spontaneous conformational change. Different paramyxoviruses may use different mechanisms of fusion triggering<sup>6-8</sup>.

Most paramyxoviruses use sialic acid-containing cell surface molecules as receptors<sup>5</sup>. By contrast, measles virus uses a protein molecule, SLAM (also called CD150), as a receptor<sup>9,10</sup>. SLAM is the prototype member of the SLAM family of receptors, which mediates important regulatory signals in immune cells and includes

2B4, CD48, CD84, CD229, CD319 and natural killer, T- and B-cell antigen (NTB-A)<sup>11,12</sup>. The SLAM family shares a similar immunoglobulin (Ig) domain-containing structural organization. SLAM is expressed on thymocytes, activated lymphocytes, mature dendritic cells, macrophages and platelets<sup>12</sup>, and is also a marker for the most primitive hematopoietic stem cells<sup>13</sup>. It acts as a self ligand, interacting with another SLAM molecule present on an adjacent cell at a low affinity ( $K_d \cong 200 \mu\text{M}$ )<sup>14</sup>. The distribution and function of SLAM may explain the tropism and immunosuppressive nature of measles virus<sup>10</sup>.

Although SLAM is the predominant receptor for wild-type, circulating field isolates of measles virus, vaccine strains of the virus use CD46 as an alternate receptor, owing to amino acid changes in the attachment protein MV-H<sup>10,15-17</sup>. An as-yet-unknown receptor molecule also exists on polarized epithelial cells, which may facilitate transmission via aerosol droplets<sup>18-20</sup>.

We and others have determined the crystal structure of the receptor-binding head domain of MV-H<sup>21,22</sup>. The structure of the MV-H-CD46 complex has also been reported recently<sup>23</sup>. The MV-H head domain forms a disulfide-linked homodimer and exhibits a six-bladed  $\beta$ -propeller fold. Here we present the crystal structure of the MV-H head domain in complex with the critical Ig domain of marmoset (*Saguinus oedipus*) SLAM at a resolution of 3.15 Å. The structure provides the molecular basis for the effectiveness of the current measles virus vaccine and a framework for structure-based antiviral drug design. Furthermore, it sheds light on how binding of MV-H to SLAM triggers the conformational change of the measles virus fusion protein (MV-F) required for membrane fusion.

<sup>1</sup>Department of Virology, Faculty of Medicine, Kyushu University, Fukuoka, Japan. <sup>2</sup>Laboratory of Biomolecular Science, Faculty of Pharmaceutical Sciences, Hokkaido University, Sapporo, Japan. <sup>3</sup>Research Center for Prevention of Infectious Diseases, Medical Institute of Bioregulation, Kyushu University, Fukuoka, Japan. <sup>4</sup>Institute for Enzyme Research, University of Tokushima, Tokushima, Japan. <sup>5</sup>Core Research for Evolutional Science and Technology, Japan Science and Technology Agency, Saitama, Japan. Correspondence should be addressed to Y.Y. (yyanagi@virology.med.kyushu-u.ac.jp) or K.M. (kmaenaka-umin@umin.net).

Received 10 May 2010; accepted 29 October 2010; published online 9 January 2011; doi:10.1038/nsmb.1969



## RESULTS

## Crystallization of the MV-H–SLAM complex

MV-H is a type II membrane protein comprised of an N-terminal cytoplasmic tail, a transmembrane region, a stalk and a C-terminal receptor-binding head domain<sup>3,5</sup>. Its receptor, SLAM, is a type I membrane protein that contains an extracellular region with two Ig-like domains (V-set and C2-set) in addition to a transmembrane region and a cytoplasmic tail<sup>11</sup>. Of these, the membrane-distal V-set Ig domain is sufficient for receptor function<sup>24</sup>. SLAM from both human and marmoset species acts as a receptor for measles virus<sup>9</sup>.

The V-set Ig domains of the human and marmoset SLAM (hSLAM-V and maSLAM-V, respectively) and the MV-H head domain were produced as described<sup>21,25</sup>, and used for crystallization (Table 1). A 1:1 complex of MV-H head (residues 149–617) and maSLAM-V crystallize and diffract to a resolution of 4.5 Å. The mixture of MV-H and hSLAM-V did not crystallize. We improved diffractions by engineering a fusion construct in which the MV-H head domain (residues 184–607) and maSLAM-V (residues 30–140 with N102H and R108Y substitutions) were connected via a 12-residue flexible linker, (Gly-Gly-Gly-Ser)<sub>3</sub>. We introduced the two substitutions in maSLAM-V (N102H and R108Y) to remove residues that were probably detrimental to crystal packing, on the basis of preliminary crystallization studies. The MV-H–maSLAM-V protein was expressed as a single chain, purified and methylated. Crystals diffracted to a resolution of 3.55 Å. An additional substitution, L482R, in MV-H further improved the diffraction to a resolution of 3.15 Å. We determined the structure of the MV-H–maSLAM-V complex by molecular replacement using an uncomplexed MV-H head domain (free MV-H)<sup>21</sup> as a search model. The bound SLAM was manually fitted into the residual electron density using the structure of CD48 as a model<sup>26</sup>.

## Overall structure of the MV-H–SLAM complex

The asymmetric unit contains two essentially identical dimers of the 1:1 MV-H–maSLAM-V complex (Fig. 1a–c). Wild-type MV-H has a six-bladed β-propeller fold and dimerizes using an intermolecular Cys154–Cys154 disulfide bond. Although the MV-H used for crystallization here does not contain Cys154, the homodimer is still formed by noncovalent interactions at the interface. Furthermore, the structure of complexed MV-H is essentially identical to that of free MV-H (r.m.s. deviation of 1.84 Å; 407 Cα atoms); Fig. 1d). Hence, no large structural change of the MV-H head domain or of its dimeric orientation occurs upon receptor binding.

The bound maSLAM-V exhibits a typical Ig-fold structure comprising the BED and AGFCC' C'' β-sheets, with a Cys32–Cys132 disulfide bond stabilizing the A-G interstrand interaction (Fig. 1a and Supplementary Fig. 1a). Previous mutational studies and the crystal structure of the free MV-H have suggested that SLAM may bind a small 'acidic patch' on the β5 sheet of MV-H<sup>21,22,27,28</sup>. The crystal structure of the complex presented here shows that although the β5 sheet forms the center of the SLAM-binding site, the complete binding site is assembled by the β4, β5 and β6 sheets at the side of the MV-H β-propeller. This site is bound by the AGFCC' C'' β-sheet of maSLAM-V (Fig. 1a,c and Supplementary Fig. 1b). The complex formed by individually expressed MV-H and maSLAM-V is essentially identical to that formed by the MV-H–maSLAM-V fusion protein, indicating that the single-chain construction does not substantially affect the structure of the complex (Supplementary Fig. 1c,d). The subsequent C2-set Ig domain of maSLAM, which was not included in our construct, can be placed continuously from the N-terminal V-set Ig domain without any steric hindrance from the bound MV-H (Fig. 1a), suggesting that the C2-set Ig domain is outside the

Table 1 Data collection and refinement statistics

	Native	MV-H–SLAM N102H R108Y fusion	MV-H L482R– SLAM N102H R108Y fusion
<b>Data collection</b>			
Space group	<i>P</i> 6 <sub>3</sub> 22	<i>P</i> 6 <sub>3</sub> 22	<i>C</i> 2
Cell dimensions			
<i>a</i> , <i>b</i> , <i>c</i> (Å)	208.1, 208.1, 182.1	209.9, 209.9, 180.5	187.7, 170.1, 110.7
$\alpha$ , $\beta$ , $\gamma$ (°)	90.0, 90.0, 120.0	90.0, 90.0, 120.0	90.0, 117.3, 90.0
Resolution (Å)	30–4.50 (4.66–4.50)	30–3.55 (3.68–3.55)	50–3.15 (3.26–3.15)
<i>R</i> <sub>merge</sub>	0.078 (0.592)	0.074 (0.498)	0.138 (0.496)
<i>I</i> / $\sigma$ <i>I</i>	15.4 (4.9)	38.6 (6.5)	10.3 (2.9)
Completeness (%)	100.0 (100.0)	99.5 (100.0)	99.5 (98.8)
Redundancy	15.5 (10.9)	20.0 (18.5)	4.6 (4.5)
<b>Refinement</b>			
Resolution (Å)	30–4.52 (4.86–4.52)	30–3.55 (3.68–3.55)	20–3.15 (3.35–3.15)
No. reflections	14,115 (2,750)	28,487 (2,808)	52,452 (8,371)
<i>R</i> <sub>work</sub> / <i>R</i> <sub>free</sub>	0.326 (0.349) / 0.338 (0.362)	0.250 (0.342) / 0.283 (0.356)	0.231 (0.305) / 0.292 (0.365)
No. atoms			
Protein	4,135	4,006	16,229
Ligand/ion	28	28	64
<i>B</i> -factors			
Protein	271.5	138.8	70.3
Ligand/ion	324.8	161.6	96.2
R.m.s. deviations			
Bond lengths (Å)	0.009	0.009	0.009
Bond angles (°)	1.5	1.5	1.5

One crystal was used for each data set. Values in parentheses are for highest-resolution shell.

MV-H-binding interface, and thus does not contribute to MV-H binding, consistent with previous domain-swapping studies<sup>24</sup>.

Notably, the highly tilted orientation of the monomers in the MV-H homodimer<sup>21</sup> suggests that the SLAM-binding interface on MV-H is located far from the viral envelope (Fig. 1a,b). Furthermore, the mode of receptor binding by MV-H is distinct from modes of receptor binding of other paramyxovirus attachment proteins and the influenza virus neuraminidase (Flu-NA), which share the six-bladed β-propeller fold (Fig. 1c and Supplementary Fig. 2). For example, the hemagglutinin–neuraminidase of parainfluenza virus 5 (PIV5–HN), the G protein of Nipah virus (NiV–G) and Flu-NA use the top of the β-propeller for binding to their receptor or ligand<sup>29–33</sup>. Of these, PIV5–HN and Flu-NA use a shallow pocket at the top to bind sialic acid, whereas NiV–G uses a wide surface area at the top to bind its receptor, ephrin B2 or ephrin B3, with a small pocket into which Phe120 of ephrin B2 or Tyr120 of ephrin B3 penetrates<sup>30,31</sup>. MV-H is unique in its use of the side of the β-propeller fold to bind its receptor SLAM.

## The interaction between MV-H and SLAM

The crystal structure shows four components of the binding interface (contact area of 1,050 Å<sup>2</sup>) between MV-H and SLAM (sites 1–4, Fig. 2a,b). Site 1 is formed by salt bridges of Asp505 and Asp507 in the proposed acidic patch of MV-H to Lys77 and Arg90 of maSLAM-V. Site 2 is formed by salt bridges of MV-H Arg533 to MV-H Asp530 and maSLAM-V Glu123 as well as two hydrophobic interactions of MV-H Phe552 and Pro554 with maSLAM-V His61 and Val63. Site 3 is an intermolecular

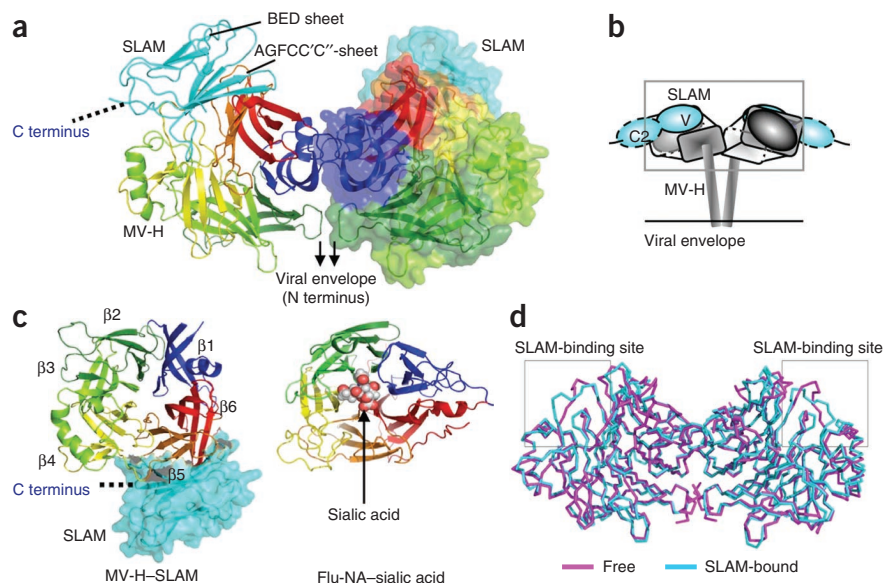


**Figure 1** Overall structure of the MV-H-SLAM complex. (a) Side view of the MV-H-maSLAM-V complex. The MV-H head domain exhibits the six-bladed  $\beta$ -propeller fold (rainbow colors) and forms a homodimer. Monomer at left, ribbon diagram; monomer at right, surface diagram. SLAM-V (cyan) exhibits a typical  $\beta$ -sandwich structure with two  $\beta$ -sheets, BED and AGFCC' sheet. (b) Schematic of the homodimer of the MV-H-SLAM complex on the viral envelope. Gray cube, MV-H head domain with its top central pocket, which is probably covered by an N-linked sugar. Cyan ovals, V-set and C2-set Ig domains of SLAM. Box, area in a. (c) MV-H-SLAM and Flu-NA-sialic acid (PDB 1NSC) complexes as viewed downward through the top central pocket of respective  $\beta$ -propellers. MV-H and Flu-NA bind to their receptors using the side and the top of the  $\beta$ -propeller, respectively. (d) Side view of the free form (magenta) of the MV-H homodimer superimposed on that of the SLAM-bound form (cyan). Box, SLAM-binding site.

$\beta$ -sheet assembled by the polypeptide backbones of the Pro191-Arg195 strand of MV-H ( $\beta 6$  sheet) and the Ser127-Phe131 strand of maSLAM-V. Site 4 is hydrophobic and has two components. The first is aromatic stacking of Tyr524, Tyr541, Tyr543 and Phe552 of MV-H with Phe119 and the Glu75-Arg130 salt bridge of maSLAM-V. The second involves hydrophobic interactions among Phe483, Tyr524, Tyr543 and Pro545 of MV-H and Asn72 and Val74 at the CC' loop region of maSLAM-V.

The host range of measles virus may be explained by key residues of SLAM at the interface shown by the crystal structure. All residues in contact with MV-H are conserved between marmoset and human SLAM except position 119 (phenylalanine in maSLAM and leucine in hSLAM)<sup>9,11</sup>. In contrast, murine SLAM, which cannot function as a receptor for measles virus<sup>24</sup>, has multiple substitutions in this region, including two key residues, His61 and Arg130. hSLAMs mutated to contain Ser61 or Ser130 lose the ability to bind MV-H, as we detected by surface plasmon resonance (SPR) analysis (Table 2), and no longer support measles virus entry (Fig. 2c). Our previous study with chimeric and mutant SLAM proteins also showed the importance of His61 in measles virus receptor function of hSLAM<sup>34</sup>. The crystal structure shows that the aromatic ring of His61 of maSLAM makes

a  $\pi$ -cation interaction with Arg533 of MV-H, which seems to stabilize the interaction of Arg533 with SLAM Glu123 (Fig. 2b, site 2). Arg130 on the G strand of maSLAM-V makes an intramolecular salt bridge with Glu75, located at the CC' loop, and also has stacking interactions with MV-H Phe552 and SLAM Phe119 (Fig. 2b, site 4). This may be the reason why the R130S substitution, but not the E75S substitution, abolishes the binding to MV-H and measles virus receptor function (Table 2 and Fig. 2c). hSLAM E123S also does not bind MV-H and does not support measles virus infection. Mutations in other SLAM residues that interact with MV-H in the crystal structure less strongly affect binding to MV-H and measles virus infection (Table 2, Fig. 2c and Supplementary Fig. 3a).

From the structure of the SLAM-V monomer in the MV-H-maSLAM-V complex, we generated a model of the physiological SLAM-SLAM dimer (Supplementary Fig. 4a) based on the reported structure of the 2B4-CD48 heterodimer<sup>35</sup>. In this model, the homophilic binding interface is located on the FCC'  $\beta$ -sheet strands

**Figure 2** Interaction between MV-H and SLAM. (a) Side view of MV-H monomer (rainbow colors) bound (right) or unbound (left) to maSLAM-V (cyan) in a ribbon diagram. Top central pocket of the MV-H  $\beta$ -propeller is covered by an N-linked sugar. The four components of the binding interface are indicated (sites 1-4). (b) Detailed views of sites 1-4 (SLAM, cyan; MV-H, red or orange depending on the blade of  $\beta$ -propeller). (c) Measles virus receptor function of SLAM mutants as examined by measles virus entry assay. Representative of three separate experiments; error bars, s.d. (d) Residues assumed important for homophilic SLAM-SLAM binding (magenta) are mapped on the SLAM structure. They are located on the FCC' strands. Residues not involved in binding as determined by SPR analysis, blue.

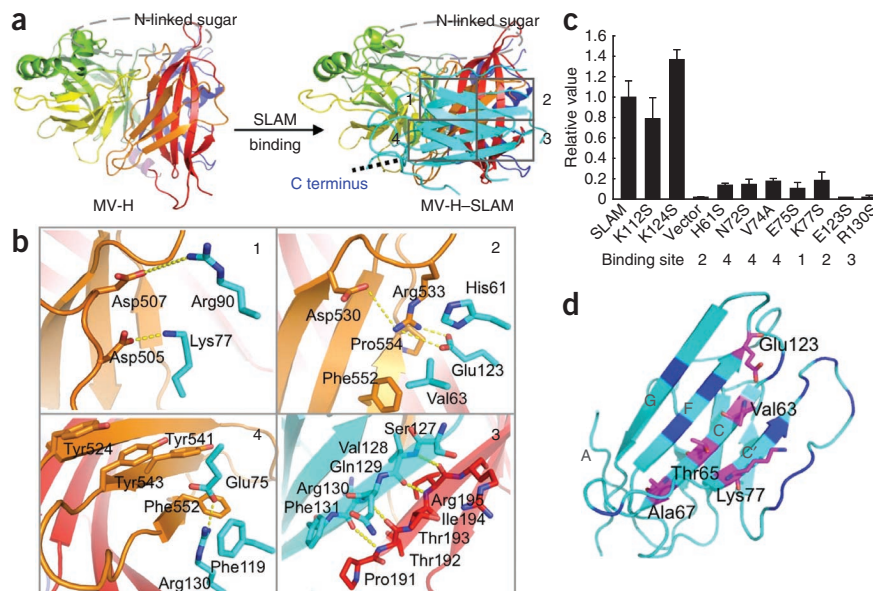


**Table 2 SPR analysis of SLAM mutants**

Analyte	Ligand	Position of mutation	$K_d$ ( $\mu\text{M}$ ) <sup>a</sup>
MV-H	SLAM	—	$0.52 \pm 0.21$
	SLAM H61S	Site 2	No binding
	SLAM N72S	Site 4	$1.6 \pm 0.17$
	SLAM V74A	Site 4	$2.0 \pm 0.087$
	SLAM E75S	Site 4	$7.7 \pm 1.1$
	SLAM K77S	Site 1	$1.7 \pm 0.12$
	SLAM E123S	Site 2	No binding
	SLAM R130S	Site 3	No binding
	SLAM N53Q	BC loop	$1.1 \pm 0.37$
SLAM	SLAM	—	$82 \pm 3.4$
	SLAM H61S	BC loop	$107 \pm 2.6$
	SLAM V63A	C strand	No binding
	SLAM T65A	C strand	No binding
	SLAM A67D	C strand	No binding
	SLAM K77S	C' strand	No binding
	SLAM E123S	F strand	No binding
	SLAM R130S	G strand	$68 \pm 0.88$

Analyte, protein injected in solution; ligand, protein immobilized on CM5 chip. SPR sensorgrams, nonlinear fitting curves and other SLAM mutants examined are shown in **Supplementary Figure 3**. <sup>a</sup> $K_d$ , mean  $\pm$  s.d.

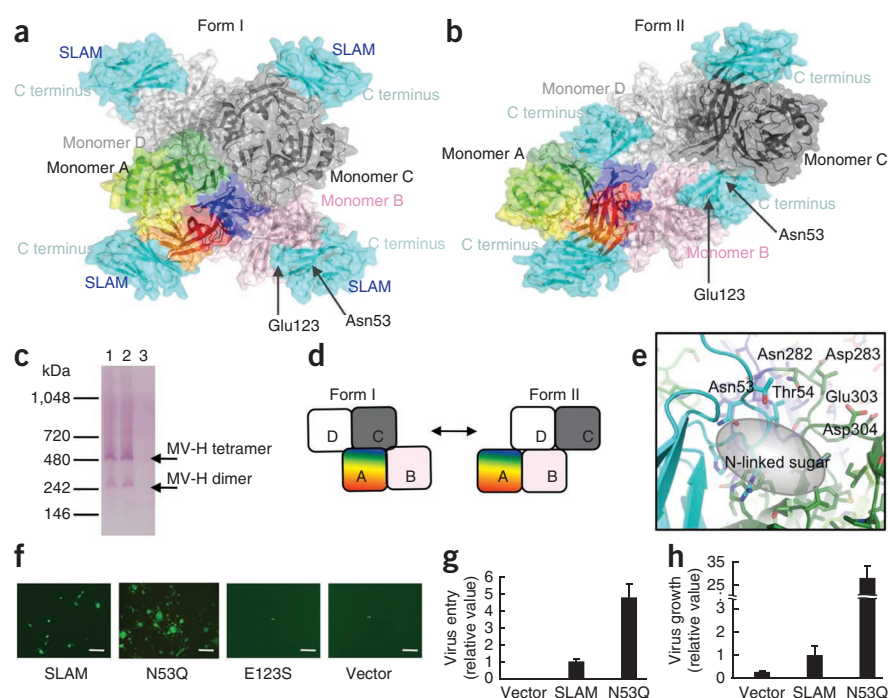
and the CC' loop (**Fig. 2d** and **Supplementary Fig. 5a,b**). Present in the interface are Val63, Thr65, Ala67, Lys77 and Glu123. These residues are conserved in human, marmoset, cow, dog, sheep and mouse SLAM, except the one at position 63, which is leucine in SLAM of the last four species (**Supplementary Fig. 4b**). Substitutions of any of these residues in hSLAM caused a loss of homophilic binding (**Table 2** and **Supplementary Fig. 3b**), validating our structural model. Notably, the SLAM-SLAM binding interface largely overlaps with the MV-H-SLAM binding interface (Lys77 and Glu123). However, the

affinity of the MV-H-SLAM interaction is >100-fold higher than that of the SLAM-SLAM interaction (**Table 2**). Thus, during measles virus entry, the MV-H-SLAM interaction should predominate over *cis* or *trans* SLAM-SLAM interactions on the host membrane.

### MV-H tetramer

When we closely examined the crystal structures, we unexpectedly found two different potential tetrameric configurations of the MV-H-SLAM complex (forms I and II; **Fig. 3a,b**). The crystal structures at a resolution of 3.55 and 4.5 Å exhibit form I, whereas the structure at a resolution of 3.15 Å shows form II. Transient transfection of the full-length MV-H into HEK293T cells also produced tetramers, as we found with blue native PAGE (BN-PAGE) and immunoblotting (**Fig. 3c**). As has been shown for Newcastle disease virus (NDV)-HN<sup>36</sup> and PIV5-HN<sup>29</sup>, the MV-H tetramer is a dimer of dimers that is arranged with two axes of two-fold symmetry. Monomers A and B form one dimer, and monomers C and D form another (**Fig. 3a,b,d**). Each dimer constituting a tetramer has essentially the same structure within and between the two forms. The overall configuration of MV-H form I is similar to those reported for NDV-HN, PIV5-HN and Flu-NA (**Supplementary Fig. 6**), although relative orientation of monomers in the dimer units varies substantially depending on the viral proteins. In form I, the MV-H monomers A and C largely form the interface of two dimers with a contact area of 1,312 Å<sup>2</sup> (**Fig. 3a,d**), and the N-terminal regions of four monomers are probably joined together, placing the stalks in the central axis (**Supplementary Fig. 6**). In contrast, the configuration of MV-H form II shifts the dimer-of-dimers interface to the boundary between monomers B and D (total contact area of 2,099 Å<sup>2</sup>; **Fig. 3b,d**). This shifted dimer-of-dimers conformation would allow the stalk regions to move laterally, leaving a large central space (**Supplementary Fig. 6**). The residue at position 482 of MV-H mutated to obtain the structure at a resolution of 3.15 Å

**Figure 3** MV-H tetramer. (**a,b**) Two forms of MV-H dimer of dimers with each monomer bound to SLAM-V. MV-H monomers A (rainbow colors) and B (light pink) form one dimer, whereas monomers C (dark gray) and D (light gray) form another. Top view of form I, **a** (3.55 Å-resolution structure). Top view of form II, **b** (3.15 Å-resolution structure). (**c**) BN-PAGE analysis of full-length MV-H. Lanes 1 and 2, MV-H of the wild-type IC-B and Edmonston vaccine strains of measles virus, respectively. Lane 3, untransfected control cells. (**d**) Schematics of form I and form II MV-H tetramers. Colors of respective monomers are the same as in **a,b**. (**e**) The MV-H (green)-SLAM (cyan) interface containing SLAM Asn53 in form II. SLAM Asn53 with an N-linked sugar (gray oval) is located close to an acidic patch in MV-H monomer A or C. (**f**) Receptor function of SLAM mutants. Representative images of HEK293 cells transiently transfected with the plasmids encoding the indicated SLAM proteins or empty plasmid (vector) and infected with enhanced GFP-expressing recombinant measles virus without the fusion block peptide, as observed with a fluorescence microscope at 48 h after infection. Scale bars, 300  $\mu\text{m}$ . (**g**) Entry efficiencies of SLAM proteins as examined by measles virus entry assay. Representative of three separate experiments; error bars, s.d. (**h**) Infection of HEK293 cells transiently transfected with plasmids encoding indicated SLAM proteins, with luciferase-expressing recombinant measles virus<sup>18</sup>. Luciferase activities were quantified at 24 h after infection. Error bars, s.d.



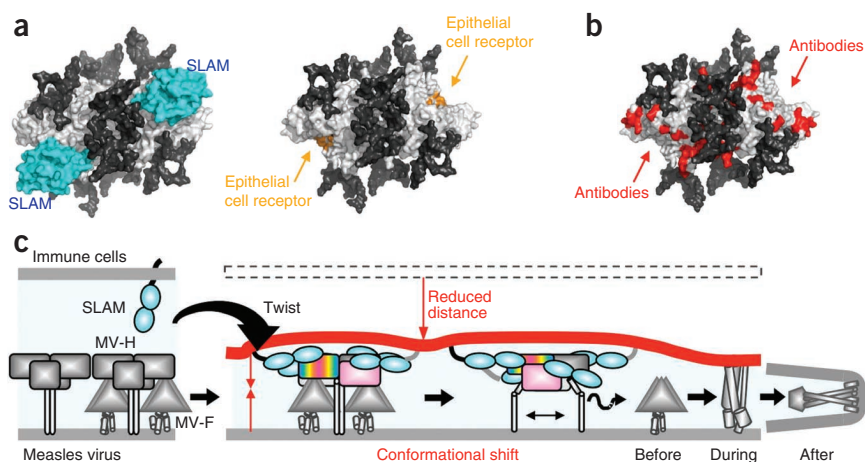


**Figure 4** Structural basis of effectiveness of measles virus vaccine and a model of measles virus-induced membrane fusion. (a) Receptor-binding sites on MV-H. Left, structure of MV-H homodimer (gray) as viewed downward from top with potential N-linked sugars (black). SLAM (cyan) binds to the uncovered exposed surface of MV-H. Right, residues in orange are probably involved in interaction with putative epithelial cell receptor, based on site-directed mutagenesis of MV-H<sup>19,20,27,28</sup>. (b) Residues in red are epitopes of monoclonal antibodies to MV-H<sup>39–41</sup>. (c) The binding of MV-H to SLAM on an immune cell in a twisted ‘head-to-head’ orientation probably reduces the distance between the viral envelope and the cell membrane. The subsequent shift of the MV-H dimer-of-dimers conformation (from I to form II) may allow MV-F to undergo successive structural changes, leading to membrane fusion.

is not located at the dimer-of-dimers interface in either form I or II, suggesting that the substitution does not greatly affect the structure.

SLAM residues His61, Asn72, Val74, Glu75, Lys77, Glu123 and Arg130 mutated in the previous section are located close to MV-H in both forms I and II, whereas Asn53, a potential N-linked glycosylation site, is located at the interface between SLAM-V and MV-H monomer A (or C) only in form II (Fig. 3a,b,e). hSLAM N53Q has lower apparent molecular masses than wild-type hSLAM (data not shown), indicating that Asn53 is indeed used as an N-linked glycosylation site. hSLAM N53Q allows increased measles virus entry (Fig. 3f,g) and larger syncytium formation owing to enhanced cell-cell fusion (Fig. 3f), which leads to higher measles virus growth, compared with wild-type SLAM (Fig. 3h). Notably, this hSLAM mutant has similar affinity for direct binding to soluble MV-H (Table 2). One interpretation of these results is that the N53Q substitution facilitates stable formation of form II by removing carbohydrates between SLAM-V and MV-H and enhances membrane fusion after receptor binding. We also found a form II-like conformation in crystal packing of the reported structure of PIV3-HN, which contained a part of the stalk region in its construct<sup>37</sup> (Supplementary Fig. 7).

## DISCUSSION

In this study, we have determined the crystal structure of MV-H bound to its primary receptor, SLAM. The structure shows the binding interface assembled by four sites (Fig. 2b). Mutagenesis studies have identified MV-H residues Ile194, Asp505, Asp507, Asp530, Arg533, Phe552 and Pro554 to be important for binding SLAM<sup>27,28,38</sup>. Our study confirms that these seven residues are indeed located at the interface. Three other residues of MV-H (Phe483, Tyr541 and Tyr543) are essential for infection of polarized epithelial cells, but not SLAM-positive immune cells<sup>19,20</sup>. These residues occur in site 4 in the crystal structure and do interact with SLAM, but on the basis of the mutagenesis data their contribution is probably not critical. The SLAM-binding interface provides a target for structure-based design of drugs

to block the MV-H–SLAM interaction. For example, a hydrophobic pocket consisting of Tyr541, Tyr543, Phe552 and Pro554 at the center of the binding interface is also a part of the putative binding site for an unidentified epithelial cell receptor. Compounds targeted to this site may block both SLAM- and epithelial cell receptor-mediated measles virus infection. A recent study of the crystal structure of MV-H bound to the CD46 molecule, a receptor used only by vaccine strains of measles virus, has shown that two sequential proline residues on the protruding loop in the N-terminal domain of CD46 have a key role in the interaction with MV-H<sup>23</sup>. The authors suggest that a similar proline-proline motif found in SLAM (Pro88–Pro89) may be involved in the recognition of MV-H. However, our study shows that these residues are not directly in contact with MV-H, but rather precede Arg90 in site 1.

In our previous report, we proposed that N-linked sugars (present on Asn168, Asn187, Asn200 and Asn215) cover large surface areas of MV-H and therefore only a limited surface area is exposed for receptor and antibody binding<sup>21</sup>. Indeed, in both the

SLAM-complexed (present study) and the uncomplexed structures of MV-H<sup>21</sup>, the glycan attached to Asn215 seems to cover the large top pocket of the  $\beta$ -propeller head domain. The complexed crystal structure shows that a large part of the MV-H surface presumably left exposed is engaged by SLAM-V (Fig. 4a). Furthermore, the binding site for the epithelial cell receptor is probably located near the SLAM-binding site<sup>19,20</sup> (Fig. 4a), as is the binding site for the CD46 receptor<sup>23</sup> (Supplementary Fig. 2). Furthermore, the epitopes for most monoclonal antibodies to MV-H<sup>39–41</sup> map here as well (Fig. 4b). Thus, all receptors and most neutralizing antibodies bind to overlapping or closely located regions on the limited exposed surface of MV-H. This may explain why a single antibody can inhibit measles virus infection mediated by different receptors<sup>18</sup>. Furthermore, the inability of measles virus to mutate or mask its exposed receptor-binding face probably explains why the virus has never escaped immune responses induced by natural infection or vaccination, and still occurs in only a single serotype<sup>3,42</sup>.

The free soluble MV-H (lacking a stalk) forms a homodimer<sup>21</sup>. Therefore, we did not expect that the MV-H–SLAM complex would exhibit a dimer of dimers (tetramer). Receptor binding could induce the formation of MV-H tetramers, as has been suggested for NDV tetramers<sup>36</sup>. However, our biochemical analysis shows that the full-length MV-H alone can form a tetramer (Fig. 3c). The stalk domain may induce tetramer formation. Indeed, free PIV5-HN containing a stalk forms a tetramer in solution and in crystals<sup>29</sup>. Henipavirus attachment G proteins containing a stalk also exist as tetrameric species<sup>43</sup>. Similarly, free intact MV-H molecules probably form dimers and tetramers on the viral envelope. This study suggests that receptor binding may facilitate MV-H tetramer formation even without the stalk region.

Partial disassembly of the dimer of dimers has been proposed as a mechanism of triggering paramyxovirus-mediated fusion, on the basis of crystal and electron microscopic structures of PIV5-HN<sup>29,44</sup>. Our results showing two forms of MV-H–SLAM tetramer

may provide the structural basis for such a model. Notably, both form I- and form II-like tetramer models can also be readily built by superimposing the reported MV-H-CD46 structure<sup>23</sup> on our structures of the MV-H-SLAM complex. Furthermore, we found that substitution of Lys54 abolishes measles virus receptor function of hSLAM without affecting its ability to bind MV-H (data not shown). Because maSLAM (used for crystallization) has a different residue at this position, we cannot determine exactly how Lys54 in hSLAM interacts with MV-H residues. However, we suppose that Lys54 is located close to MV-H in form II, but not in form I (Fig. 3a,b,e). Along with the data for the N53Q substitution (Fig. 3f-h and Table 2), the results suggest that form II has an important role in membrane fusion after receptor binding. Taken together, these results indicate that the shift of MV-H dimer of dimers could act as a mechanism of fusion triggering.

Our results may suggest the following sequence of events during measles virus-induced membrane fusion (Fig. 4c). The MV-H dimer of dimers is associated with the MV-F trimer on the viral envelope. At the host cell surface, the AGFCC' C''  $\beta$ -sheet of SLAM-V binds to the side of the MV-H  $\beta$ -propeller, which is located upward from the virus surface because of the tilted orientation of the  $\beta$ -propeller. SLAM probably has straight V- and C2-set ectodomains, like those of other SLAM family receptors<sup>45,46</sup>. This structural arrangement inevitably renders the orientation of the V- and C2-set domains parallel rather than perpendicular in relation to the host membrane. The interaction substantially reduces the distance between the viral and host membranes (~140 Å if the stalk region of MV-H forms a straight  $\alpha$ -helix<sup>44,47</sup>), setting the stage for the subsequent conformational change of MV-F and membrane fusion. Then, the configuration of the dimer of dimers may shift (from form I to form II), changing the orientation of the stalk regions, allowing MV-F to refold and interact with the target cell membrane and eventually leading to membrane fusion.

The dimer of dimers seems to have a weak interaction<sup>29,44</sup>, and its conformational shift probably requires a small amount of energy and is probably induced by receptor binding. Such a shift of the attachment protein dimer of dimers may either actively induce the conformational change of the fusion protein required for membrane fusion or release the fusion protein from the clamp to facilitate its spontaneous conformational change, depending on the paramyxovirus species.

## METHODS

Methods and any associated references are available in the online version of the paper at <http://www.nature.com/nsmb/>.

**Accession codes.** Protein Data Bank: Coordinates have been deposited for form I (4.5- and 3.55-Å resolution) and form II (3.15-Å resolution) of the MV-H-maSLAM complex (accession codes 3ALZ, 3ALW and 3ALX, respectively). GenBank: cDNA sequence of the measles virus Edmonston tag strain H protein, AB583749.

*Note: Supplementary Information is available on the Nature Structural & Molecular Biology website.*

## ACKNOWLEDGMENTS

We thank the beamline staff of Photon Factory (Tsukuba, Japan) and SPring8 (Hyogo, Japan) for technical help during data collection. We also thank M.A. Billeter (Institute of Molecular Biology, University of Zürich) for reagents, M. Takeda, I. Tanaka, K. Inaba, K. Mihara, T. Oka, H. Aramaki, K. Tokunaga, M. Kajikawa, K. Kuroki and K. Sasaki for discussion and E.O. Saphire for reviewing the manuscript. This work was supported by grants from the Ministry of Education, Culture, Sports, Science and Technology of Japan and the Ministry

of Health, Labor and Welfare of Japan. T.H. is supported by the Japan Society for the Promotion of Science Research Fellowship for Young Scientists.

## AUTHOR CONTRIBUTIONS

T.H., K.M. and Y.Y. designed the research; T.H. and J.K. prepared and crystallized MV-H-SLAM complexes; T.H. and M.K. carried out binding, BN-PAGE and measles virus infection assays; T.H., T.O., N.M. and K.M. determined the crystal structures; T.H., K.M. and Y.Y. wrote the paper.

## COMPETING FINANCIAL INTERESTS

The authors declare no competing financial interests.

Published online at <http://www.nature.com/nsmb/>.

Reprints and permissions information is available online at <http://npg.nature.com/reprintsandpermissions/>.

- Bryce, J., Boschi-Pinto, C., Shibuya, K. & Black, R.E. WHO estimates of the causes of death in children. *Lancet* **365**, 1147–1152 (2005).
- Moss, W.J. & Griffin, D.E. Global measles elimination. *Nat. Rev. Microbiol.* **4**, 900–908 (2006).
- Griffin, D.E. in *Fields Virology* (eds. Knipe, D.M. *et al.*) 1551–1585 (Lippincott Williams & Wilkins, Philadelphia, 2007).
- Harrison, S.C. Viral membrane fusion. *Nat. Struct. Mol. Biol.* **15**, 690–698 (2008).
- Lamb, R.A. & Parks, G.D. in *Fields Virology* (eds. Knipe, D.M. *et al.*) 1449–1496 (Lippincott Williams & Wilkins, Philadelphia, 2007).
- Iorio, R.M. & Mahon, P.J. Paramyxoviruses: different receptors—different mechanisms of fusion. *Trends Microbiol.* **16**, 135–137 (2008).
- Smith, E.C., Popa, A., Chang, A., Masante, C. & Dutch, R.E. Viral entry mechanisms: the increasing diversity of paramyxovirus entry. *FEBS J.* **276**, 7217–7227 (2009).
- Connolly, S.A., Leser, G.P., Jardetzky, T.S. & Lamb, R.A. Bimolecular complementation of paramyxovirus fusion and hemagglutinin-neuraminidase proteins enhances fusion: implications for the mechanism of fusion triggering. *J. Virol.* **83**, 10857–10868 (2009).
- Tatsuo, H., Ono, N., Tanaka, K. & Yanagi, Y. SLAM (CDw150) is a cellular receptor for measles virus. *Nature* **406**, 893–897 (2000).
- Yanagi, Y., Takeda, M., Ohno, S. & Hashiguchi, T. Measles virus receptors. *Curr. Top. Microbiol. Immunol.* **329**, 13–30 (2009).
- Cocks, B.G. *et al.* A novel receptor involved in T-cell activation. *Nature* **376**, 260–263 (1995).
- Schwartzberg, P.L., Mueller, K.L., Qi, H. & Cannons, J.L. SLAM receptors and SAP influence lymphocyte interactions, development and function. *Nat. Rev. Immunol.* **9**, 39–46 (2009).
- Kiel, M.J. *et al.* SLAM family receptors distinguish hematopoietic stem and progenitor cells and reveal endothelial niches for stem cells. *Cell* **121**, 1109–1121 (2005).
- Mavaddat, N. *et al.* Signaling lymphocytic activation molecule (CDw150) is homophilic but self-associates with very low affinity. *J. Biol. Chem.* **275**, 28100–28109 (2000).
- Naniche, D. *et al.* Human membrane cofactor protein (CD46) acts as a cellular receptor for measles virus. *J. Virol.* **67**, 6025–6032 (1993).
- Dörig, R.E., Marciel, A., Chopra, A. & Richardson, C.D. The human CD46 molecule is a receptor for measles virus (Edmonston strain). *Cell* **75**, 295–305 (1993).
- Manchester, M., Liszewski, M.K., Atkinson, J.P. & Oldstone, M.B. Multiple isoforms of CD46 (membrane cofactor protein) serve as receptors for measles virus. *Proc. Natl. Acad. Sci. USA* **91**, 2161–2165 (1994).
- Takeda, M. *et al.* A human lung carcinoma cell line supports efficient measles virus growth and syncytium formation via a SLAM- and CD46-independent mechanism. *J. Virol.* **81**, 12091–12096 (2007).
- Tahara, M. *et al.* Measles virus infects both polarized epithelial and immune cells by using distinctive receptor-binding sites on its hemagglutinin. *J. Virol.* **82**, 4630–4637 (2008).
- Leonard, V.H. *et al.* Measles virus blind to its epithelial cell receptor remains virulent in rhesus monkeys but cannot cross the airway epithelium and is not shed. *J. Clin. Invest.* **118**, 2448–2458 (2008).
- Hashiguchi, T. *et al.* Crystal structure of measles virus hemagglutinin provides insight into effective vaccines. *Proc. Natl. Acad. Sci. USA* **104**, 19535–19540 (2007).
- Colf, L.A., Joo, Z.S. & Garcia, K.C. Structure of the measles virus hemagglutinin. *Nat. Struct. Mol. Biol.* **14**, 1227–1228 (2007).
- Santiago, C., Celma, M.L., Stehle, T. & Casasnovas, J.M. Structure of the measles virus hemagglutinin bound to the CD46 receptor. *Nat. Struct. Mol. Biol.* **17**, 124–129 (2010).
- Ono, N., Tatsuo, H., Tanaka, K., Minagawa, H. & Yanagi, Y. V domain of human SLAM (CDw150) is essential for its function as a measles virus receptor. *J. Virol.* **75**, 1594–1600 (2001).
- Reeves, P.J., Callewaert, N., Contreras, R. & Khorana, H.G. Structure and function in rhodopsin: high-level expression of rhodopsin with restricted and homogeneous N-glycosylation by a tetracycline-inducible N-acetylglucosaminyltransferase I-negative HEK293S stable mammalian cell line. *Proc. Natl. Acad. Sci. USA* **99**, 13419–13424 (2002).

26. Evans, E.J. *et al.* Crystal structure and binding properties of the CD2 and CD244 (2B4)-binding protein, CD48. *J. Biol. Chem.* **281**, 29309–29320 (2006).
27. Massé, N. *et al.* Measles virus (MV) hemagglutinin: evidence that attachment sites for MV receptors SLAM and CD46 overlap on the globular head. *J. Virol.* **78**, 9051–9063 (2004).
28. Vongpunsawad, S., Oezgun, N., Braun, W. & Cattaneo, R. Selectively receptor-blind measles viruses: Identification of residues necessary for SLAM- or CD46-induced fusion and their localization on a new hemagglutinin structural model. *J. Virol.* **78**, 302–313 (2004).
29. Yuan, P. *et al.* Structural studies of the parainfluenza virus 5 hemagglutinin-neuraminidase tetramer in complex with its receptor, sialyllactose. *Structure* **13**, 803–815 (2005).
30. Bowden, T.A. *et al.* Structural basis of Nipah and Hendra virus attachment to their cell-surface receptor ephrin-B2. *Nat. Struct. Mol. Biol.* **15**, 567–572 (2008).
31. Xu, K. *et al.* Host cell recognition by the henipaviruses: crystal structures of the Nipah G attachment glycoprotein and its complex with ephrin-B3. *Proc. Natl. Acad. Sci. USA* **105**, 9953–9958 (2008).
32. Varghese, J.N., Laver, W.G. & Colman, P.M. Structure of the influenza virus glycoprotein antigen neuraminidase at 2.9 Å resolution. *Nature* **303**, 35–40 (1983).
33. Burmeister, W.P., Ruigrok, R.W. & Cusack, S. The 2.2 Å resolution crystal structure of influenza B neuraminidase and its complex with sialic acid. *EMBO J.* **11**, 49–56 (1992).
34. Ohno, S., Seki, F., Ono, N. & Yanagi, Y. Histidine at position 61 and its adjacent amino acid residues are critical for the ability of SLAM (CD150) to act as a cellular receptor for measles virus. *J. Gen. Virol.* **84**, 2381–2388 (2003).
35. Velikovsky, C.A. *et al.* Structure of natural killer receptor 2B4 bound to CD48 reveals basis for heterophilic recognition in signaling lymphocyte activation molecule family. *Immunity* **27**, 572–584 (2007).
36. Zaitsev, V. *et al.* Second sialic acid binding site in Newcastle disease virus hemagglutinin-neuraminidase: implications for fusion. *J. Virol.* **78**, 3733–3741 (2004).
37. Lawrence, M.C. *et al.* Structure of the haemagglutinin-neuraminidase from human parainfluenza virus type III. *J. Mol. Biol.* **335**, 1343–1357 (2004).
38. Navaratnarajah, C.K. *et al.* Dynamic interaction of the measles virus hemagglutinin with its receptor signaling lymphocytic activation molecule (SLAM, CD150). *J. Biol. Chem.* **283**, 11763–11771 (2008).
39. Hu, A., Sheshberadaran, H., Norrby, E. & Kovamees, J. Molecular characterization of epitopes on the measles virus hemagglutinin protein. *Virology* **192**, 351–354 (1993).
40. Fournier, P. *et al.* Antibodies to a new linear site at the topographical or functional interface between the haemagglutinin and fusion proteins protect against measles encephalitis. *J. Gen. Virol.* **78**, 1295–1302 (1997).
41. Ertl, O.T., Wenz, D.C., Bouche, F.B., Berbers, G.A. & Muller, C.P. Immunodominant domains of the Measles virus hemagglutinin protein eliciting a neutralizing human B cell response. *Arch. Virol.* **148**, 2195–2206 (2003).
42. Ruigrok, R.W. & Gerlier, D. Structure of the measles virus H glycoprotein sheds light on an efficient vaccine. *Proc. Natl. Acad. Sci. USA* **104**, 20639–20640 (2007).
43. Bossart, K.N. *et al.* Receptor binding, fusion inhibition, and induction of cross-reactive neutralizing antibodies by a soluble G glycoprotein of Hendra virus. *J. Virol.* **79**, 6690–6702 (2005).
44. Yuan, P., Leser, G.P., Demeler, B., Lamb, R.A. & Jardetzky, T.S. Domain architecture and oligomerization properties of the paramyxovirus PIV 5 hemagglutinin-neuraminidase (HN) protein. *Virology* **378**, 282–291 (2008).
45. Chothia, C. & Jones, E.Y. The molecular structure of cell adhesion molecules. *Annu. Rev. Biochem.* **66**, 823–862 (1997).
46. Cao, E. *et al.* NTB-A receptor crystal structure: insights into homophilic interactions in the signaling lymphocytic activation molecule receptor family. *Immunity* **25**, 559–570 (2006).
47. Paal, T. *et al.* Probing the spatial organization of measles virus fusion complexes. *J. Virol.* **83**, 10480–10493 (2009).

## ONLINE METHODS

**Construction of expression plasmids.** The DNA fragments encoding the MV-H head domain (Asp149–Arg617 or Ser184–Arg617) were amplified by PCR using the p(+)/MV2A (a gift from M.A. Billeter) containing the antigenomic full-length cDNAs of the Edmonston tag strain of measles virus<sup>48</sup> as a template. These amplified fragments were cloned into a derivative of the expression vector pCA7 (ref. 49) as described<sup>21</sup>. This derivative vector contains the signal and His<sub>6</sub> tag sequences up- and downstream of the protein-coding sequence, respectively, and allows high-level expression of secreted proteins. The fragment encoding maSLAM-V including the authentic signal sequence (Met1–Gln140) was amplified by PCR from the pCAGB95aSLAM plasmid that contains the full-length cDNA of maSLAM<sup>9</sup>, and cloned into pCA7 that contains a His<sub>6</sub> tag sequence downstream of the protein-coding sequence. To express single-chain MV-H–maSLAM-V fusion proteins, a (Gly-Gly-Gly-Ser)<sub>3</sub> linker was inserted between the sequence encoding the MV-H head domain (Ser184–Thr607) and that encoding maSLAM-V (Met30–Gln140). To increase stability and solubility of the expressed proteins, several mutations were introduced at various positions of the fusion construct. The crystals examined in this study were obtained using the constructs in which mutations were introduced at position 482 of MV-H (L482R) and/or positions 102 and 108 of maSLAM-V (N102H R108Y). The L482R substitution was used, as change from leucine to a basic residue at position 482 of MV-H increases SLAM-dependent cell fusion (data not shown), and this substitution has been found in a clinical isolate of measles virus (genotype D1). The N102H and R108Y substitutions of maSLAM-V were adopted to remove an N-linked glycosylation site and prevent the charge repulsion, respectively, based on the structure at a resolution of 4.5 Å. Tyrosine was used to replace arginine at position 108, as CD48 has tyrosine at the corresponding position. For binding assays, a fragment encoding the ectodomain of hSLAM (Gly26–Ala239) was amplified by PCR using the pCAGSLAM containing the full-length cDNA of hSLAM<sup>9</sup>, and cloned into pCA7 containing the signal and influenza virus hemagglutinin tag sequences and biotinylation tag sequence up- and downstream of the protein-coding sequence, respectively. For measles virus entry and infection assays, a fragment encoding hSLAM (Gly26–Ser335) was amplified and cloned into pCA7 containing the signal and hemagglutinin tag sequences upstream of the protein-coding sequence.

**Expression, purification and modification of proteins.** To prepare soluble proteins, expression plasmids encoding the appropriate proteins were transiently transfected using polyethylenimine, together with the plasmid encoding the SV40 large T antigen, into 90% confluent HEK293S GnTI<sup>-</sup> cells<sup>21,25</sup>. The cells were cultured in DMEM supplemented with 10% (v/v) FBS (FBS), L-glutamine and nonessential amino acids (Gibco). The concentration of FBS

was lowered to 2% (v/v) immediately after transfection. Supernatants containing the expressed proteins were harvested 5 d after transfection, and mixed with the Ni<sup>2+</sup>-NTA affinity column binding buffer (50 mM NaH<sub>2</sub>PO<sub>4</sub>, 150 mM NaCl, 10 mM imidazole, pH 8.0). The proteins were purified via Ni<sup>2+</sup>-NTA affinity, followed by Superdex 200GL 10/300 (GE Healthcare) gel filtration chromatography. To introduce methylation in lysine residues, the purified protein was treated with 20 mM dimethyl-boron and 40 mM formaldehyde at 4 °C overnight, and repurified by size-exclusion chromatography. For SPR analysis, expression plasmids encoding the proteins with the biotinylation tag at the C terminal were transiently transfected into HEK293 cells cultured in OPTI-MEM medium. At 4 d after transfection, the culture media were centrifuged, sterile-filtered, and treated with biotin-protein ligase (Avidity) in 20 mM Tris-HCl, pH 8.0 at 30 °C for 2 h. Supernatants containing the biotinylated proteins were subsequently dialyzed against HEPES-buffered saline (HBS)-P buffer (10 mM HEPES, 150 mM NaCl, 0.005% (v/v) surfactant P20, pH 7.4) (GE Healthcare) and injected onto the streptavidin-attached sensor chip on which only the biotinylated proteins were immobilized.

**Crystallization of MV-H in complex with SLAM-V.** Crystals were grown by the sitting- or floating-drop vapor diffusion using Fluorinert (Hampton Research) at 20 °C (ref. 50). A 1:1 mixture of MV-H<sub>149–617</sub> and maSLAM-V<sub>1–140</sub> containing 0.2 μl each of protein (9.3 mg ml<sup>-1</sup>, in 20 mM imidazole, pH 8.0, 100 mM NaCl) and mother liquor (0.1 M MES, pH 6.5, 0.75 M Li<sub>2</sub>SO<sub>4</sub>) was set up for crystallization. Crystals of this complex diffract only to a resolution of 4.5 Å. Drops of the single-chain MV-H<sub>184–607</sub>–maSLAM<sub>30–140</sub> N102H R108Y containing 1 μl each of protein (12.7 mg ml<sup>-1</sup>, in 20 mM imidazole, pH 8.0, 100 mM NaCl) and mother liquor (0.1 M imidazole pH 5.8, 0.5 M (NH<sub>4</sub>)<sub>2</sub>SO<sub>4</sub>, 0.7 M Li<sub>2</sub>SO<sub>4</sub>, 3% (v/v) ethylene glycol) produced crystals that diffract to a resolution of 3.55 Å. To obtain higher-resolution structures, the single-chain MV-H<sub>184–607</sub>–maSLAM-V<sub>30–140</sub> N102H R108Y complex was prepared. Crystallization was achieved in the solution containing 1 μl each of protein (14.0 mg ml<sup>-1</sup>, in 20 mM imidazole, pH 8.0, 100 mM NaCl) and mother liquor (0.1 M imidazole, pH 8.3, 0.5 M (NH<sub>4</sub>)<sub>2</sub>SO<sub>4</sub>, 0.7 M Li<sub>2</sub>SO<sub>4</sub>, 0.05 M lithium acetate, 1% (v/v) ethylene glycol). These crystals diffract to a resolution of 3.15 Å.

Structure determination, binding analysis, assays for measles virus entry and infection and BN-PAGE are described in the **Supplementary Methods**.

48. Radecke, F. *et al.* Rescue of measles viruses from cloned DNA. *EMBO J.* **14**, 5773–5784 (1995).
49. Takeda, M. *et al.* Long untranslated regions of the measles virus M and F genes control virus replication and cytopathogenicity. *J. Virol.* **79**, 14346–14354 (2005).
50. Adachi, H. *et al.* Application of a two-liquid system to sitting-drop vapour-diffusion protein crystallization. *Acta Crystallogr. D Biol. Crystallogr.* **59**, 194–196 (2003).